J. Fluid Mech. (1972), *vol.* 51, *part* 2, *pp.* 233–272
Printed in Great Britain

The stability of an incompressible two-dimensional wake

By G. E. MATTINGLY AND W. O. CRIMINALE†
Department of Civil and Geological Engineering, Princeton University

(Received 28 May 1970)

The growth of small disturbances in a two-dimensional incompressible wake has been investigated theoretically and experimentally. The theoretical analysis is based upon inviscid stability theory wherein small disturbances are considered from both temporal and spatial reference frames. Through a combined stability analysis, in which small disturbances are permitted to amplify in both time and space, the relationship between the disturbance characteristics for the temporal and spatial reference frames is shown. In these analyses a quasi-uniform assumption is adopted to account for the continuously varying mean-velocity profiles that occur behind flat plates and thin airfoils. It is found that the most unstable disturbances in the wake produce transverse oscillations in the mean-velocity profile and correspond to growing waves that have a minimum group velocity.

Experimentally, the downstream development of the wake of a thin airfoil and the wave characteristics of naturally amplifying small disturbances are investigated in a water tank. The disturbances that develop are found to produce transverse oscillations of the mean-velocity profile in agreement with the theoretical prediction. From the comparison of the experimental results with the predictions for the characteristics of the most unstable waves via the temporal and spatial analyses, it is concluded that the stability analysis for the wake is to be considered solely from the more realistic spatial viewpoint. Undoubtedly, this conclusion is also applicable to other highly unstable flows such as jets and free shear layers.

In accordance with the disturbance vorticity distribution as determined from the spatial model, a description of the initial development of a vortex street is put forth that contrasts with the description given by Sato & Kuriki (1961).

1. Introduction

One of the fundamental flows in fluid mechanics that has remained unexplained is that of the high Reynolds number wake development behind a moving streamlined body. This applies both to streamlined bodies having an axis of symmetry parallel to the direction of motion, and to 'two-dimensional' bodies which are

† Present address: Department of Oceanography and Geophysics Group, University of Washington, Seattle.

symmetric with respect to a plane oriented parallel to the direction of motion. It is this latter case that will be considered here. The search for a mechanism whereby a flow that began as a boundary layer attached to the surface of the body leaves it and develops downstream to form the well-known von Kármán vortex street has consistently attracted attention for many years. Many experimental studies have been made that have terminated with the advancement of hypotheses to account for the observations. Except in a few cases, however, where critical assumptions have been required to derive meaningful conclusions, the problem has not been theoretically described. Generally speaking, therefore, our understanding of the subject remains limited.

Several gross features of a wake of this type are clear. For example, the motion is effectively two-dimensional, unsteady, and incompressible. Once the Reynolds number is large enough, the details of the particular body involved (whether a circular cylinder or a flat plate) tend to be lost and the ultimate wake is characterized by a shedding frequency f. The non-dimensional equivalent of the frequency is the Strouhal number S_t (where $S_t = fD/U_\infty$, D is the wake width and U_∞ is the free-stream velocity), and for a circular cylinder its value has been observed to be 0·21 with only a weak dependence on the Reynolds number. Finally, for streamlined bodies, the laminar wake flow fields have been predicted analytically by similarity solutions which athough not strictly valid in the very near wake do indicate decent agreement with experimental results.

A notable investigation directed toward an understanding of the wake behind a thin flat plate has been made by Sato & Kuriki (1961). These authors were concerned primarily with the transition of the wake and its far downstream characteristics. Their findings led them to speculate on the origins of these characteristics. Essentially, they visualized the initially laminar wake flow to be characterized by a configuration of oppositely rotating vortices lying along the centre-plane of the wake which ultimately become unstable. These vortices then mutually interact as they move downstream in the near wake and displace each other transversely to yield the classical von Kármán street. By combining some simple calculations with the measurements, Sato & Kuriki were able to synthesize a reasonable description and lend support to this hypothesis.

The present work is concerned with the very near wake of the flat plate beginning at the trailing edge and thus is complementary to the downstream wake measurements made by Sato & Kuriki. Specifically, this very near wake region is found to be linear in the sense that the intensity of the fluctuations is small thereby lending itself naturally to linearized stability analysis throughout. In this paper, both a theoretical and an experimental study of this very near wake are presented. A mechanism to describe the initial stages of Kármán vortex street development based upon the conclusions of this work is suggested. In short, it is conjectured that the flow farther downstream is a consequence of the flow in the very near wake.

The theory presented for the naturally developing disturbances involves a combination of both spatial and temporal analyses. The differences found using these two viewpoints are quite sensitive to mean-velocity profile shape (see Betchov & Criminale 1966). As a consequence, a quasi-uniform assumption was

adopted to approximate the changing mean-velocity profile with downstream direction. Gaster & Davey (1968) made spatial calculations on the original Sato & Kuriki wake for comparison with the known temporal values. They concluded that a transformation using the group velocity could properly show equivalence between the two approaches. The particular case chosen for computation here, however, suffers from the same misleading assumption that the profiles preceding this station can yield no new behaviour. It will be shown that there are differences between temporal and spatial stability analyses in the very near wake; experimental evidence shows that the spatial viewpoint gives superior predictions for disturbance characteristics. Consequently, it is concluded that all future stability analyses in highly unstable flows such as jets and force shear layers should use the relevant spatial method.

2. Experiment

2.1. *Description of facility*

The experiment was conducted in the John E. Nicholson Tilting Flume Facility of the Lewis F. Moody Hydrodynamics Laboratory of Princeton University and is described in detail by Mattingly (1968). By using screens and honeycombs the turbulence level was reduced to 0.04 % for the range of mean velocities considered. The wake generating body was an NACA 0003 symmetric airfoil shape with 12 in. chord length and maximum thickness scaled to 0.375 in. The Reynolds number ranged between $1{\cdot}6 \times 10^4$ and $4{\cdot}0 \times 10^4$.

Crude velocity measurements were made using the hydrogen-bubble flow visualization technique; detailed surveys were made using hot-wire anemometry where the sensor position was accurate to within 0·001 in. and 0·002 in. in the transverse and longitudinal directions respectively. The present wake, as seen by the hydrogen-bubble technique, is shown in figure 1 (plate 1). A survey of the near wake of the body confirmed that it is two-dimensional and spanwise uniform.

2.2. *Wake survey of perturbation characteristics*

The general aspects of the amplitudes and frequencies of the non-dimensionalized (with respect to the free-stream velocity) longitudinal perturbation velocity $\tilde{u}$ under natural amplification are shown in the fluctuation map comprising figure 2 (plates 2–4). Oscillographic records of anemometer response are shown for various wake stations both on the wake centre-plane and just off the axis of symmetry. The amplitude levels of the longitudinal perturbation velocity are recorded beside the respective oscillograph; the time interval between dots is 0·1 sec.

The solid lines in figure 2 delineate the wake boundaries. The dotted boundaries are intended to indicate the approximate extremities of the regions where (i) the level of oscillation is greater than or equal to 1·0 % and (ii) the second harmonic of the oscillation occurs. Note that precise boundaries cannot be given for the extremities of these regions either in naturally excited fluid flows or in artificially excited transition experiments. Note also the irregularity of the naturally excited signal. When oscillographs from artificially excited oscillations (for

example, Sato & Kuriki 1961; Freymuth 1966) are compared with those in the present study, it is discovered that the natural oscillations exhibited less regularity with regard to the frequency and amplitude of the fluctuations.

It is interesting to note the extremely small perturbation level in the wake region very near the trailing edge. At wake station $x/L = 0{\cdot}2$, where L is the chord length, the perturbation is found to be approximately 1·0 % of the free-stream velocity. This 1·0 % perturbation level occurs off the wake centre-plane. On the wake centre-plane, a similar 1·0 % perturbation level signal is not obtained until $x/L = 0{\cdot}25$. The form of the oscillation is that of a two-dimensional sinusoidal velocity fluctuation that grows in the downstream direction. It will be seen later that this growth is exponential.

A search was conducted to determine the beginning of the second harmonic of the oscillation and the region containing it. The second harmonic was found to occur on the wake centre-plane as near as $x/L = 0{\cdot}33$ downstream of the trailing edge of the airfoil. As previously defined, and shown by the oscillographs, the region that contained the second harmonic is indicated by the slender shaded area in the figure.

The intended goal is the prediction of the initial downstream development of the perturbation quantities given the assumptions involved. This is possible if we recognize from the fluctuation map that there is a range in the near wake region, from $x/L = 0$ to $x/L = 0{\cdot}3$, that can be well defined and where linearized stability analysis can be applied.

2.3. *Velocity measurements*

The calculation of eigenvalues for the present wake required a detailed determination of the wake velocity field. Along the wake centre-plane, the mean velocity was measured both in the near wake region and beyond. These results are shown in figure 3, where a comparison is made with the theoretical results of Goldstein (1929) and analogous experimental measurements of Sato & Kuriki (1961). In light of the present results, which indicate a markedly reduced longitudinal variation in the wake centre-plane velocity in the near wake region, it is surprising to find such good agreement between the experimental results of Sato & Kuriki and the theoretical results of Goldstein. The Goldstein result is achieved using boundary-layer approximations. Although these approximations are applicable in the far wake, it is clear from the large longitudinal gradient of the centre-plane velocity that such an assumption is questionable in the near wake. It is felt that perhaps the loudspeaker stimulation used in the Sato & Kuriki experiment to excite selected disturbance frequencies could account for the difference between their results and the present measurements.

To facilitate the computer calculation of the eigenvalues, the wake velocity profiles were smoothed, using the hyperbolic function

$$\frac{U-U_\infty}{U_c-U_\infty} = \operatorname{sech}^2 \sigma Y,$$

where $Y = y/b$ and U_c is the value of U on the centre-line. The quantity b is the half-breadth thickness, which increases very slightly with downstream distance

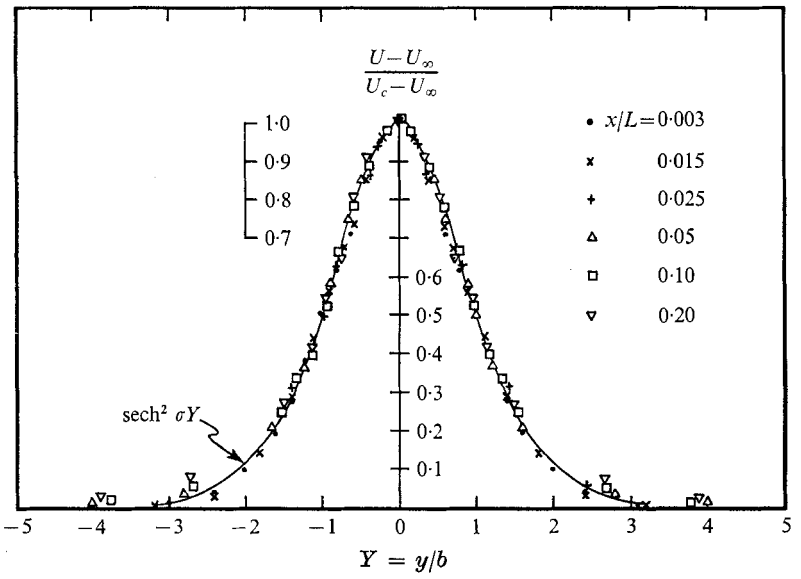

FIGURE 3. Mean defect velocity distribution.

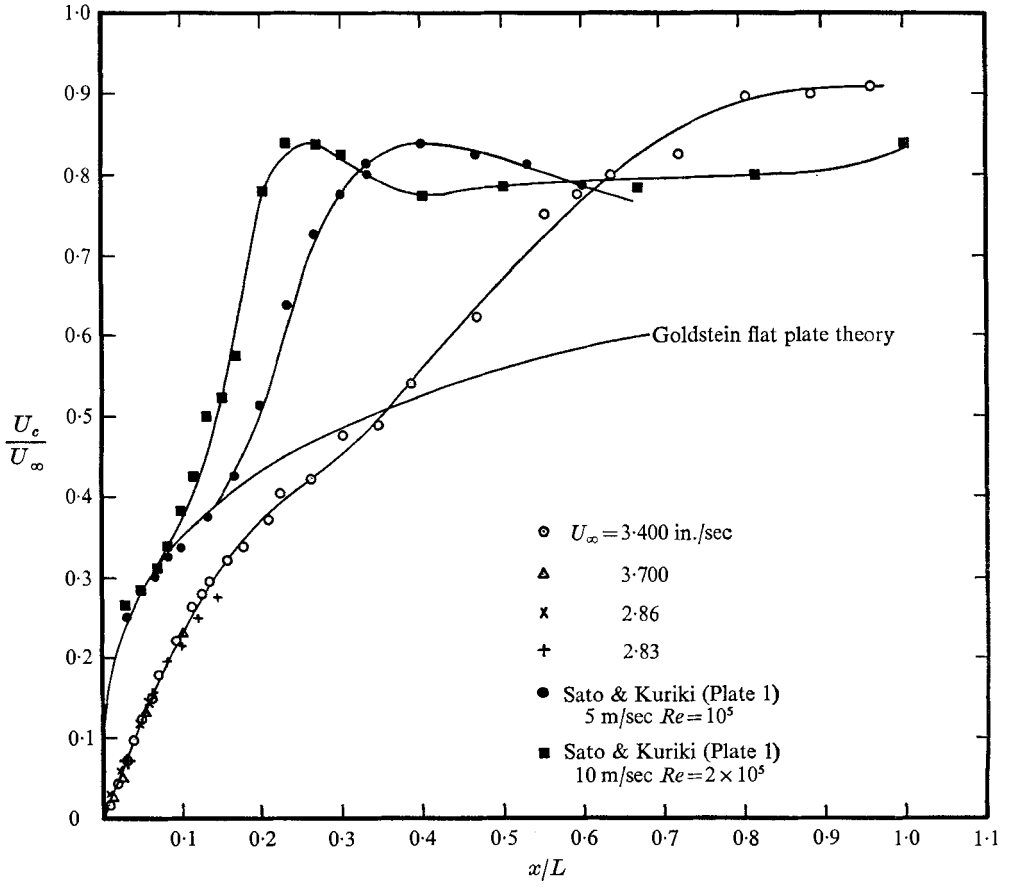

FIGURE 4. Longitudinal variation of the wake centre-plane velocity, U_c.

from a value of $b = 0{\cdot}125$ in. to $b = 0{\cdot}130$ in. between wake stations $x/L = 0{\cdot}003$ and 0·30. The quantity σ is chosen so that $(U-U_\infty)/(U_c-U_\infty) = \frac{1}{2}$ at $Y = \pm 1$. The result is shown in figure 4. Since the spatial eigenvalue results of Betchov & Criminale (1966) seem to indicate a sensitive dependence upon wake centre-plane velocity, the curve fit procedure matches this quantity directly, leaving small deviations from the smoothing curves to occur at the outer edges of the wake.

3. Theory

3.1. *Development of equations*

Theoretical considerations are based upon two-dimensional linearized stability theory. Non-dimensionalization of velocities is achieved by taking as the unit of velocity the free-stream velocity U_∞. Co-ordinates x (in the flow direction) and y (perpendicular to the flow direction) and t (time) are non-dimensionalized using the half-breadth thickness b of the mean flow profile to obtain $X = x/b$, $Y = y/b$, and $T = U_\infty t/b$. The pressure is non-dimensionalized using the product ρU_∞^2, where ρ is the fluid density. Consequently, in non-dimensional variables, the composite fluid motion is described by

$$\begin{aligned} u(X,Y,T) &= U(Y)+\tilde{u}(X,Y,T),\\ v(X,Y,T) &= \tilde{v}(X,Y,T),\\ p(X,Y,T) &= P(X)+\tilde{p}(X,Y,T), \end{aligned}$$

where tildes denote the disturbance quantities.

The linear equations of motion allow solutions of the form

$$\begin{aligned} \tilde{u}(X,Y,T) &= \mathrm{Re}\,\mathbf{u}(Y)\,e^{i(\alpha X-\omega T)},\\ \tilde{v}(X,Y,T) &= \mathrm{Re}\,\mathbf{v}(Y)\,e^{i(\alpha X-\omega T)},\\ \tilde{p}(X,Y,T) &= \mathrm{Re}\,\mathbf{p}(Y)\,e^{i(\alpha X-\omega T)}. \end{aligned}$$

Viscous effects are excluded,† and thus the governing equation becomes the Rayleigh equation obtained from continuity and momentum considerations. With mean flow quantities extracted it is written

$$(U-c)(\mathbf{v}''-\alpha^2\mathbf{v})-U''\mathbf{v} = 0, \tag{3.1}$$

where U is the mean velocity profile being analysed. Primes denote derivatives with respect to Y; the relation $\omega = \alpha c$ has also been used. The problem is completed by establishing the boundary conditions which require that the solutions be bounded for $Y \to \pm\infty$. These conditions are denoted here by

$$\mathbf{v}'(\pm\infty) \mp \mathbf{v}(\pm\infty) = (0,0), \tag{3.2}$$

where the double argument notation refers to the real and imaginary parts of the complex amplitude.

† The neutral curve for a two-dimensional wake has been determined by Curle (1957) and by Taneda (1963) for a wide range of Reynolds numbers. It is concluded from these curves that at large values of Reynolds number, viscosity has only a dampening effect on all wavy disturbances. Furthermore, at large Reynolds numbers, disturbance characteristics are found to be essentially independent of viscosity.

When the mean-velocity profile is symmetrical with respect to $Y = 0$, the Rayleigh equation admits both symmetrical and antisymmetrical disturbances. Symmetrical disturbances, which will be referred to as mode I,† satisfy

$$\mathbf{v}(0) = (1, 0), \quad \mathbf{v}'(0) = (0, 0), \tag{3.3}$$

while antisymmetrical disturbances, referred to as mode II,‡ satisfy

$$\mathbf{v}(0) = (0, 0), \quad \mathbf{v}'(0) = (1, 0). \tag{3.4}$$

From continuity, symmetry in $\mathbf{v}(Y)$ implies antisymmetry in $\mathbf{u}(Y)$ and vice versa. Solutions exist only when the eigenvalues α and c satisfy the appropriate characteristic equations: $F_{\mathrm{I}}(\alpha, \omega) = 0$ for mode I or $F_{\mathrm{II}}(\alpha, \omega) = 0$ for mode II.

By virtue of the symmetry of the mean-velocity profile $U(Y)$, we confine our attention to the semi-infinite interval $(0, +\infty)$ and undertake the calculations of the α and c pairs satisfying the appropriate conditions at $Y = 0$ and $Y = +\infty$. Numerical methods are used to determine, separately, the symmetric and antisymmetric solutions to the Rayleigh equation; the details can be found in Mattingly (1968). Using this numerical approach an infinite number of discreet pairs of α and ω values can be found for both mode I and mode II disturbances.

3.2. *Temporal stability*

It has been the convention to consider the frequency ω (for the phase velocity c) as a complex quantity and the wavenumber α as real. In this way, the stability analysis provides a dispersion relation that determines the sign of the imaginary part of ω for a given α. For $\omega_i > 0$, the disturbance grows exponentially in time and is termed a temporally unstable disturbance. Selection of the disturbance that is most unstable in time is based upon the maximum positive value of ω_i. According to the linearized theory, it is this disturbance, whether it is symmetric or antisymmetric, that will temporally dominate all others in the wake. To determine this dominant disturbance, we consider a superposition of the infinity of symmetric temporal disturbances in the form

$$\tilde{v}_{\mathrm{I}}(X, Y, T) = \mathrm{Re}\{\sum_n \mathbf{v}_{\mathrm{I}}[Y; \alpha_n, \omega(\alpha_n)]\, e^{i[\alpha_n X - \omega(\alpha_n) T]}\}, \tag{3.5}$$

where the subscript n refers to all mode I disturbances for which α is a real quantity. The notation $\mathbf{v}_{\mathrm{I}}[Y; \alpha_n, \omega(\alpha_n)]$ refers to the complex eigenfunction that is a function of Y alone, once the value α_n is specified and the corresponding $\omega(\alpha_n)$ is determined in accordance with the characteristic equation $F_{\mathrm{I}}(\alpha, \omega) = 0$. This superposition is the actual disturbance motion present in the wake as a result of the imposition of symmetry conditions at $Y = 0$. Similarly, the superposition of antisymmetrical disturbances is written

$$\tilde{v}_{\mathrm{II}}(X, Y, T) = \mathrm{Re}\{\sum_n \mathbf{v}_{\mathrm{II}}[Y; \alpha_n, \omega(\alpha_n)] e^{i[\alpha_n X - \omega(\alpha_n) T]}\}, \tag{3.6}$$

where the notation is that described above. The most unstable disturbance is found by comparing the exponential growth rates of the dominant symmetrical and antisymmetrical disturbances.

† Sometimes referred to as the sinuous mode.

‡ Otherwise known as the varicose mode.

3.3. *Spatial stability*

When the wavenumber is considered complex, $\alpha = \alpha_r + i\alpha_i$, and the angular frequency is constrained to be real; the imaginary part of α is then a measure of the growth of the disturbance in the x direction and must be negative for instability – hence the term spatial stability. The requirement that ω is a real quantity implies that

$$\omega_i = \alpha_i c_r + \alpha_r c_i = 0.$$

In either formulation the disturbance phase velocity is $c_p = \omega_r/\alpha_r$.

In the case of spatial stability, the symmetrical and antisymmetrical disturbance motions are written

$$\tilde{v}_{\mathrm{I}}(X, Y, T) = \mathrm{Re}\{\sum_n \mathbf{v}_{\mathrm{I}}[Y; \alpha(\omega_n), \omega_n] e^{i[\alpha(\omega_n)X - \omega_n T]}\}, \tag{3.7}$$

$$\tilde{v}_{\mathrm{II}}(X, Y, T) = \mathrm{Re}\{\sum_n \mathbf{v}_{\mathrm{II}}[Y; \alpha(\omega_n), \omega_n] e^{i[\alpha(\omega_n)X - \omega_n - T]}\} \tag{3.8}$$

where the subscript n now refers to those disturbances for which ω_n is real. Of all these disturbances, the most unstable is that characterized by the minimum negative value of α_i.

To compare temporal theoretical and experimentally determined amplification rates, the disturbance phase velocity $c_p = \omega_r/\alpha_r$ ($c_p = c_r$ in temporal formulation) has been used by many investigators to transform temporal results into spatial stability quantities. When time and space are related through $X = c_p T$, the resultant spatial amplification rate is

$$\omega_{iS} = \alpha c_i / c_p,$$

where the S subscript implies spatial. The actual amplification rate in the temporal framework is $\omega_{iT} = \alpha c_i$. If the disturbance phase velocity is the same for all disturbance wavenumbers, or simply if the wave system is non-dispersive, then this is the proper transformation. However, in a dispersive system where travelling waves that have nearly the same wavelength and frequency are superposed, one finds that groups of wave packets are formed. These groups travel with a group velocity defined as

$$U_{\mathrm{group}} = \partial\omega_r/\partial\alpha_r.$$

It has been shown by Gaster (1963) that for small rates of amplification the disturbance frequencies determined from the temporal framework are approximately equal to those of the spatial analysis. Later, Gaster (1965, 1968) concluded that for large amplification rates the analysis should be done spatially. However, despite this fact, spatial stability analyses have only recently received attention, and consequently theoretical versus experimental agreement of the amplification rates in highly amplified flows is consistently poor.

3.4. *Combined stability*

For completeness, the case of complex wavenumber, complex phase velocity, and complex frequency is termed combined stability to denote disturbances that can grow in both time and space. The generalized α, c and $\omega = \alpha c$ determined

under these conditions contain the restricted eigenvalues of the previously described temporal and spatial cases. Having these generalized eigenvalues permits a search procedure for the combined general values to be started through interpolation. Moreover, it is through these combined stability results that the relationship between the temporal and spatial cases is shown.

For instance, it has been shown by Gaster (1963) that in cases where the amplification rate is small, the temporal and spatial growths are related through the group velocity by

$$\omega_{iS} = \alpha_r c_{iT} / U_{\text{group},T}. \tag{3.9}$$

Gaster & Davey (1968) then applied this group velocity transformation to the wake profile used by Sato & Kuriki (1961) and found the results to be quite similar to their phase velocity transformed amplification rates. That is, the amplification rates found by Sato & Kuriki were actually temporal results that were transformed into spatial quantities using the phase velocity. The particular profile used for their linearized stability analysis is one for which the amplification rates are quite small. This accounts for the agreement between these two results. However, it will be shown below that amplification rates are not small throughout the near wake region where the linearized analysis is pertinent. In fact, significant differences will be found between actual spatial results and temporal results obtained using the group velocity transformation.

Gaster (1968) examined the saddle-point singularities found by Betchov & Criminale (1966) in their jet and wake eigenvalue calculations. By considering the analyticity of the characteristic function $E_{\text{I}}(\alpha, \omega)$, Gaster used a series expansion to show that the singularities must occur and the influence they exert on the motion results from a pulse input. This motion is found to be dominated by a disturbance having an amplification in both time and space proportional to

$$\exp -[\alpha_i^* X - \omega_i(\alpha^*) T]$$

where the asterisks refer to the co-ordinates of the saddle-point singularity. Given this result, Gaster found that the maximum amplification with respect to time arises when $\alpha_i = 0$, and similarly that the maximum spatial growth occurs when the saddle point lies on the line $\omega_i = 0$.

This maximum spatial growth rate is found by transforming the saddle-point co-ordinates onto the $\omega_i = 0$ contour. To do this, a series expansion of the characteristic function $F_{\text{I}}(\alpha, \omega)$ is used to express the relation $\omega = \omega(\alpha)$ in the neighbourhood of the saddle point as

$$\omega - \omega^* = \tfrac{1}{2}(\alpha - \alpha^*)^2 F_{\text{I}\alpha\alpha}(\alpha^*, \omega^*) / F_{\text{I}\omega}(\alpha^*, \omega^*), \tag{3.10}$$

where α is a double-valued function of ω, and the subscripts α, ω refer to the partial derivatives of $F(\alpha, \omega)$. Therefore, the purely spatial growth rate is written

$$\operatorname{Im} \alpha_S = \operatorname{Im} \{\alpha^* \pm [-2(\omega_S - \omega^*) F_{\text{I}\omega}(\alpha^*, \omega^*) / F_{\text{I}\alpha\alpha}(\alpha^*, \omega^*)]^{\frac{1}{2}}\}, \tag{3.11}$$

where Im denotes the imaginary part of the complex number and the subscript S means spatial, i.e. $\omega_{iS} = 0$.

3.5. *Quasi-uniform assumption*

The velocity measurements shown in figure 4 reveal that the wake-velocity profiles in the near wake region are suitably smoothed by the square of hyperbolic secant function. In addition, the longitudinal variation of the wake centre-plane velocity U_c is shown in figure 3 to deviate markedly from the theoretical assumption that the mean velocity is a function of Y only. Given this experimental result, a quasi-uniform assumption is now adopted whereby a series of mean-velocity profiles are selected throughout the wake region where disturbance amplitudes are small. The eigenvalue computation is then performed, using each successive wake profile individually with the hope that the combined result will predict the effect of longitudinal variations due to the continuously changing mean profiles. Certainly this procedure is an improvement upon the usual practice. This has consisted of selecting a single mean-velocity profile for which eigenvalues are computed and compared with the experimental measurements made throughout the fluid flow where disturbance levels comply with the linear theory.

3.6. *Neutral eigenvalues*

Working with the assumption that both the wavenumber α and the phase velocity are real quantities, it is possible to calculate the neutral eigenvalues for mode I and II disturbances. Following Betchov & Criminale (1967), these are found to be $\alpha = 1{\cdot}762$, $\omega = 0{\cdot}587$, and $c = 0{\cdot}333$ for mode I disturbances for the wake profile at $x/L = 0$. Characteristics for mode II disturbances are $\alpha = 0{\cdot}880$, $\omega = 0{\cdot}293$, and $c = 0{\cdot}333$.

In addition, it can be shown that non-trivial solutions to the Rayleigh equation exist for mode I and II disturbances characterized by the eigenvalues

$$\alpha = \omega = c = 0.$$

Consequently, for both mode I and II disturbances, we have two solutions to equation (3.1) satisfying the appropriate boundary conditions. These eigenvalues will be found to be the intersections of the $\alpha_i = 0$ temporal stability line and the $\omega_i = 0$ spatial stability line. For this reason, the above four sets of eigenvalues could be termed double neutral eigenvalues. The non-trivial double neutral eigenvalues are interesting because the critical layer is determined from the neutral phase velocity.

A very convenient eigenvalue transformation can be formulated through the form of the Rayleigh equation and the particular wake mean-velocity profile. Once a set of values α_1 and c_1 have been found for a specific wake profile, say $U_c = 0$, then the corresponding set of values α_1 and $c(U_c)$ can be determined for any other wake profile using

$$c(U_c) = \frac{c_1 - 1}{1 - U_c} + 1. \tag{3.12}$$

This transformation applies only to the temporal and combined stability eigenvalue results; there is no analogous transformation for the purely spatial stability analysis. However, using this procedure, considerable computing time

is saved by initiating the spatial eigenvalue search procedure with excellent choices obtained via interpolation between the copious combined stability eigenvalues.

3.7. *Eigenfunctions*

The solutions to the governing equation are obtained numerically. With selected eigenvalue results, the eigenfunctions are computed as follows. Taking $\mathbf{v}(Y)$ as an example, where ω is real and α is complex, the actual disturbance has an amplitude

$$|\mathbf{v}(Y)| = [\mathbf{v}(Y)\,\mathbf{v}^*(Y)]^{\frac{1}{2}}$$

and a phase

$$-\pi \leqslant \theta_{\mathbf{v}}(Y) = \tan^{-1}\frac{\mathbf{v}(Y)-\mathbf{v}^*(Y)}{i[\mathbf{v}(Y)+\mathbf{v}^*(Y)]} < \pi.$$

Therefore

$$\tilde{v}(X, Y, T) = \mathrm{Re}\{|\mathbf{v}(Y)|e^{i\theta}\,e^{-\alpha_i X}\,e^{i\alpha_r X - i\omega T}\}. \tag{3.13}$$

Averaged quantities will be of interest. For the spatial reference frame, the pertinent average is the time average defined by

$$\overline{\tilde{v}^2(X, Y)} = \lim_{T_0\to\infty}\frac{1}{T_0}\int_0^{T_0}\tilde{v}^2(X, Y, T)\,dT = \tfrac{1}{2}\mathbf{v}(Y)\,\mathbf{v}^*(Y)\,e^{-2\alpha_i X}. \tag{3.14}$$

The Reynolds stress is the mean-cross product and is defined by

$$\tau = -\overline{\rho\tilde{u}\tilde{v}} = -\tfrac{1}{4}[\mathbf{u}^*(Y)\,\mathbf{v}(Y)+\mathbf{u}(Y)\,\mathbf{v}^*(Y)]\,e^{-2\alpha_i X}. \tag{3.15}$$

At successive wake stations, transverse distributions of the Reynolds stress will be examined from the temporal and spatial stability results. In these distributions, the exponential factor will be excluded for scale reasons that will be discussed shortly.

4. Wake profiles

4.1. *Initial wake profile – mode* I *disturbances*

Adopting the quasi-uniform assumption, a wake centre-plane velocity

$$U_c = 0{\cdot}0012$$

is obtained from figure 3 for the wake station $x/L = 0{\cdot}003$. For this wake profile, the mode I eigenvalue results plotted in the complex ω plane for various values of complex α are presented in figure 5. These eigenvalues illustrate graphically the complex and explicit relationship $\omega = \omega(\alpha)$ that is also written implicitly and referred to as the characteristic equation for mode I disturbances $F_{\mathrm{I}}(\alpha, \omega) = 0$. The temporal stability contour, labelled $\alpha_i = 0$, contains unstable mode I disturbances having wavenumbers in the range $0 < \alpha_r < 1{\cdot}762$ with angular frequencies $0 < \omega_r < 0{\cdot}590$. The corresponding range of temporal amplification rate is $0 < \omega_i < 0{\cdot}140$.

The disturbance wave system is a dispersive one, and a temporal to spatial transformation made using the group velocity U_{group} leads to the disturbance

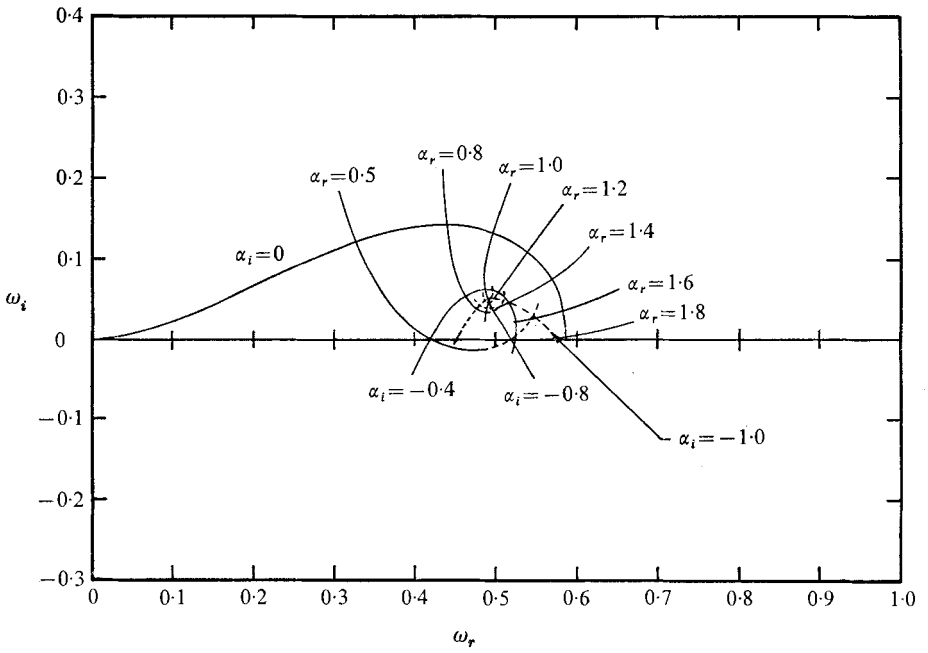

FIGURE 5. Combined stability eigenvalue results: mode I disturbances. $x/L = 0{\cdot}003$.

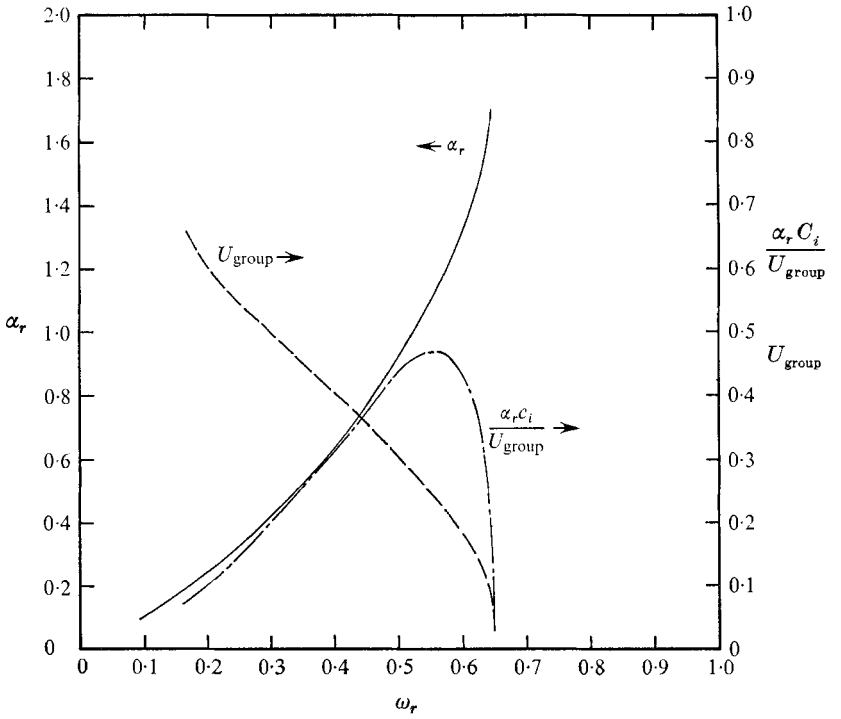

FIGURE 6. Transformed temporal stability eigenvalue results: mode I disturbances. $x/L = 0{\cdot}003$.

wavenumber α_r and the spatial amplification rate $\alpha_r c_i/U_{\text{group}}$ presented as functions of frequency ω_r in figure 6. The most unstable disturbance has a spatial amplification rate of $\alpha_r c_i/U_{\text{group}} = 0{\cdot}625$. The corresponding wavenumber and frequency are $\alpha_r = 1{\cdot}300$ and $\omega_r = 0{\cdot}550$ respectively.

Figure 5 indicates that as α_r increases along the constant α_i lines labelled $\alpha_i = 0$ or $\alpha_i = -0{\cdot}4$, curved-clockwise contours are traced about the point $\omega = (0{\cdot}49, 0{\cdot}049)$. Conversely, as α_r increases along the line $\alpha_i = -1{\cdot}0$, a counter-clockwise contour is traced about $\omega = (0{\cdot}49, 0{\cdot}049)$. Consequently, in the neighbourhood of this particular point, the relationship $\alpha = \alpha(\omega)$ is double-valued. With the exception of the neighbourhood of this point, lines of constant α_r and α_i are found to intersect orthogonally, indicating the analyticity of the functions $\omega = \omega(\alpha)$ and $\alpha = \alpha(\omega)$. The relationship between ω and α in the neighbourhood of the point is clarified by the plot of these same eigenvalue results in the α plane where ω_r and ω_i are constant. This plot, displayed in figure 7, reveals the explicit relationship $\alpha = \alpha(\omega)$ to be a saddle point. To analyse figures 5 and 7 from the spatial point of view, attention is focused on the mode I disturbances for which $\omega_i = 0$. In this framework, it is recalled that the disturbances only oscillate in time and grow or decay exponentially with downstream distance according to the imaginary part of the wavenumber α_i. Furthermore, we restrict the following discussion to downstream-moving waves and groups of waves, i.e. those having positive phase and group velocities.

Taking the superposition

$$\sum_n \mathbf{v}_{\mathrm{I}}[Y;\, \alpha(\omega_n),\, \omega_n]\, e^{i[\alpha(\omega_n)X - \omega_n T]}$$

we consider only positive values of ω_r and α_r and proceed to extract the most highly amplified eigenmode. In figure 7 we find two distinct contours for which $\omega_i = 0$. Both of these contours are portrayed in figure 5 by the eigenvalues lying along the ω_r axis. Considering the $\omega_i = 0$ contour in figure 7 along which both α_r and ω_r increase from zero, the group velocity $U_{\text{group}} = \partial\omega_r/\partial\alpha_r$ is found to decrease to zero at the frequency $\omega_r = 0{\cdot}492$. As ω_r is increased farther along this contour, the group velocity becomes negative, indicating that these groups of waves are moving upstream and are damped by virtue of their negative values of α_i.

On the other $\omega_i = 0$ contour in figure 7, waves having $\omega_r > 0{\cdot}492$ are found to be downstream moving with positive group velocities. For frequency in the interval $0{\cdot}492 < \omega_r < 0{\cdot}590$, the imaginary parts of the appropriate wavenumbers are negative, indicating disturbance amplification with downstream distance. For $\omega_r > 0{\cdot}590$, disturbances are damped as shown by the sign change of α_i in figure 5. On this same $\omega_i = 0$ contour when $\omega_r < 0{\cdot}492$, the group velocity is again found to be negative, indicating upstream-moving groups of waves that are damped by virtue of their negative values of α_i. Therefore, two separate contours for downstream-moving groups of waves having exponential amplification are found in the wake. Accordingly, it is noted that no stability prediction is immediately evident for disturbances having wavenumbers in the interval $0{\cdot}52 < \alpha_r < 1{\cdot}59$. Two disturbances, each having frequencies $\omega_r = 0{\cdot}492$, with wavenumbers $\alpha_r = 0{\cdot}52$ and $\alpha_r = 1{\cdot}59$, are predicted to have purely spatial

amplification rates, $\alpha_i = -0{\cdot}70$. In the previous temporal stability analysis, a continuous spectrum of disturbance wavenumbers is predicted to be unstable in the spatial sense. Consequently, the superposition (see equation (3.7)) is made continuous in wavenumber by utilizing the connecting path consisting of the combined stability eigenvalues along the $\omega_r = 0{\cdot}492$ contour in figure 7. In this manner, we will select from the continuous spectrum of disturbances the wave-

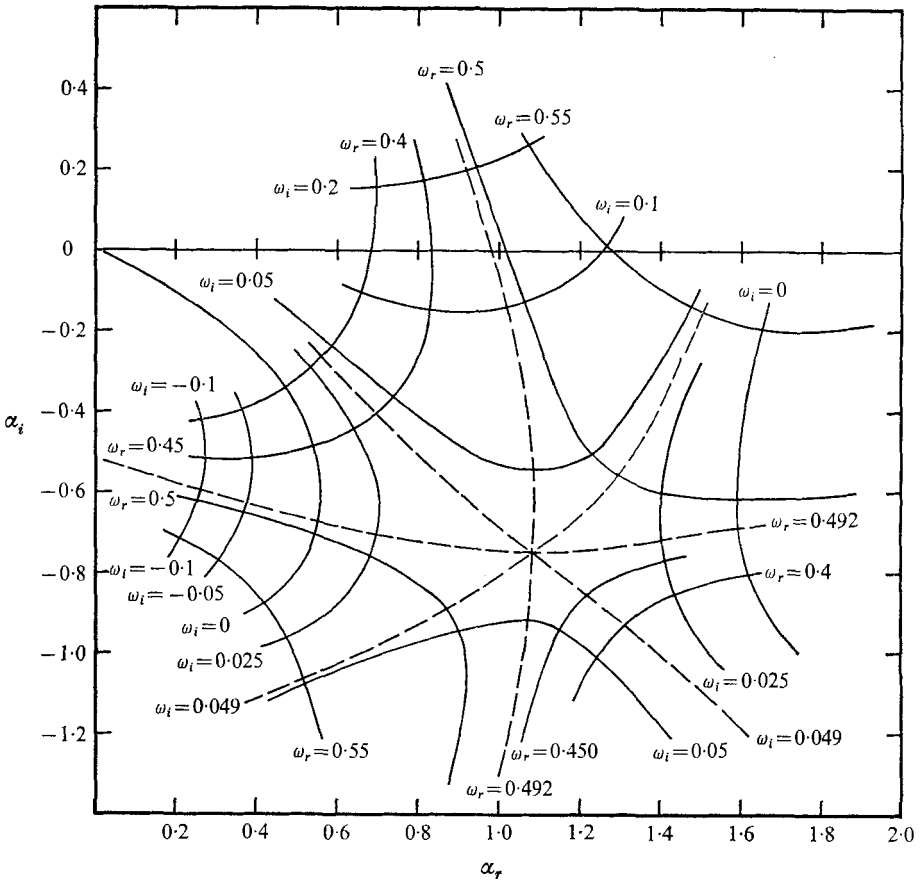

FIGURE 7. Combined stability eigenvalue results: mode I disturbances. $x/L = 0{\cdot}003$.

number and angular frequency for the most highly amplified wave. This selection is then governed by the point on the contour having the largest negative ordinate. Figure 7 shows this point to be the saddle point. Since it lies on the combined stability contour, the most highly amplified disturbance is predicted to have growth in both time and space. This wave has wavenumber $\alpha_r = 1{\cdot}09$, frequency $\omega_r = 0{\cdot}492$, and an amplification of $\alpha_i = -0{\cdot}75$ and $\omega_i = 0{\cdot}049$, which are the co-ordinates of the saddle point (α^*, ω^*). The relationship between ω and α in the neighbourhood of the saddle point is used to determine the variation in α_i that occurs as ω_i is reduced to zero while ω_r remains constant. In this way, the strictly spatial growth of the saddle-point disturbance is evaluated.

The relationship $\omega = \omega(\alpha)$ in the neighbourhood of the saddle point is given by equation (3.10). Since numerical values for $F_{\mathrm{I}\alpha\alpha}(\alpha^*\omega^*)$ and $F_{\mathrm{I}\omega}(\alpha^*\omega^*)$ are not available, the transformation is performed graphically using figure 7. From the saddle point $(\alpha^*\omega^*)$, we find that either path along the $\omega_r = 0{\cdot}49$ contour as $\omega_i \to 0$ affects an identical change in the value α_i, namely $\alpha_i \to -0{\cdot}70$ as $\omega_i = 0$.

It is important to note that such a graphical procedure is equivalent to fabricating a velocity that prescribes the temporal to spatial transformation. As the group velocity at the saddle point is zero, we take the pertinent velocity

$$U^* = \frac{\omega - \omega^*}{\alpha - \alpha^*} = -\tfrac{1}{2}(\alpha - \alpha^*)\frac{F_{\mathrm{I}\alpha\alpha}(\alpha^*, \omega^*)}{F_{\mathrm{I}\omega}(\alpha^*, \omega^*)} \tag{4.1}$$

as that used to relate time and space by $X = \mathrm{Re}\{U^*\}T$. The purely spatial growth is then

$$\exp\left(-[\alpha_i^* - \omega_i^*/\mathrm{Re}\{U^*\}]X\right).$$

The eigenvalue results for the strictly spatial analyses will be found with successive wake profiles to have continuity in both angular frequency and wavenumber. As a consequence, the most highly amplified disturbance is found without resorting to the combined stability eigenvalues and transforming saddle-point co-ordinates back to purely spatial stability results.

4.2. *Initial wake profile – mode* II *disturbances*

With the wake centre-plane velocity $U_c = 0{\cdot}0012$, the temporal, spatial and combined stability eigenvalues are found for mode II disturbances and are shown in figure 8. The saddle-point influence is not as apparent in the previous results.†

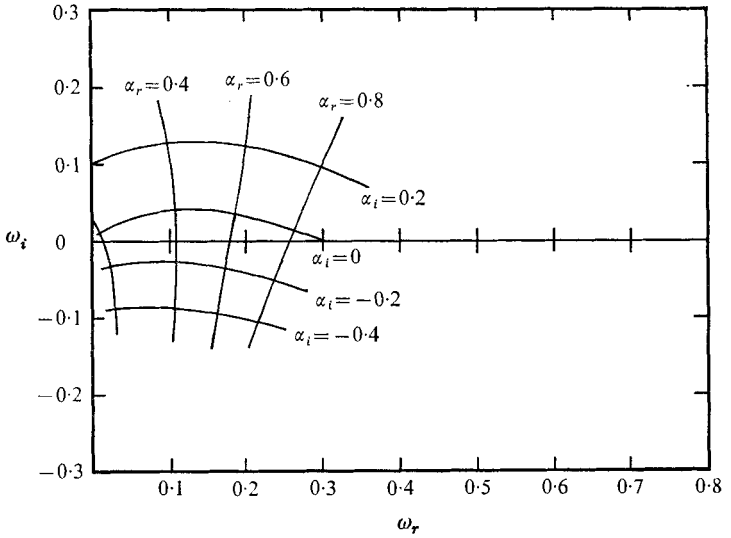

FIGURE 8. Combined stability eigenvalue results: mode II disturbances. $x/L = 0{\cdot}003$.

† Cost considerations precluded the computation of eigenvalues in both forms, i.e. $\omega = \omega(\alpha)$ and $\alpha = \alpha(\omega)$. The exception is the initial wake profile where eigenvalues for mode I were computed in both forms to clarify the nature of the saddle point. However, the presentation of eigenvalue results in the form $\omega = \omega(\alpha)$ will be sufficient to clarify the stability analyses.

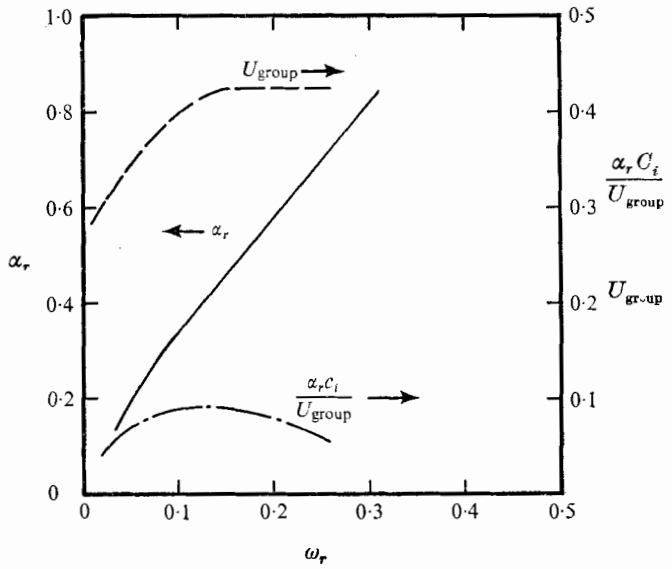

FIGURE 9. Transformed temporal stability eigenvalue results: mode II disturbances. $x/L = 0{\cdot}003$.

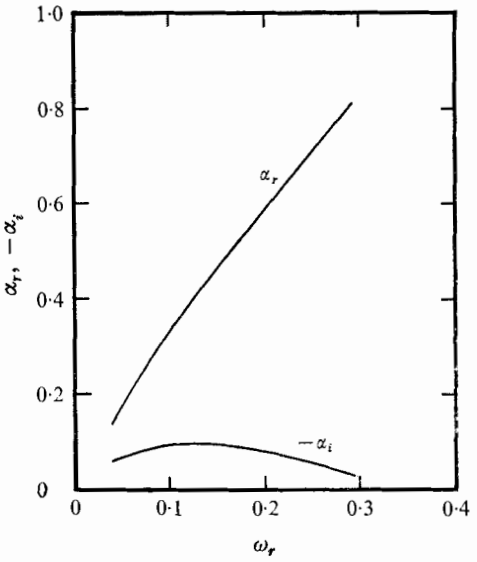

FIGURE 10. Spatial stability eigenvalue results: mode II disturbances. $x/L = 0{\cdot}003$.

To analyse the results in figure 8 in the temporal fashion, we again apply the group velocity transformation, which results in the eigenvalues shown in figure 9. The most highly amplified mode is characterized by $\alpha_r = 0{\cdot}40$, $\omega_r = 0{\cdot}130$ and $\alpha_r c_i / U_{\text{group}} = 0{\cdot}08$.

Figure 10 presents the strictly spatial stability eigenvalues for mode II disturbances in this initial wake profile. The results reveal that the disturbance which

will dominate all others in this wake profile is that having $\alpha_r = 0{\cdot}40$, $\omega_r = 0{\cdot}110$, $\alpha_i = -0{\cdot}11$. A comparison of these spatial results with those of the transformed temporal analysis confirms Gaster's (1963) conclusion that the group velocity transformation is valid, provided the amplification rates are small. A similar comparison of the mode I results indicates marked differences in the two predictions.

From the most highly amplified characteristics for mode I and II waves, it is concluded that mode I disturbance having $\alpha_r = 1{\cdot}09$, $\omega_r = 0{\cdot}492$ will dominate all other eigenmodes at the wake station $x/L = 0{\cdot}003$ by virtue of its maximum spatial amplification rate $\alpha_i = -0{\cdot}70$. It is this eigenmode that can be expected to exist in the real wake.

4.3. *Subsequent wake profiles*

The next downstream wake station chosen is $x/L = 0{\cdot}02$, where the wake centre-plane velocity $U_c = 0{\cdot}0532$. The combined stability eigenvalues for mode I disturbances are shown in figure 11. The saddle point, which originally appeared above the ω_r axis, has now moved down and is located just below this axis. As a

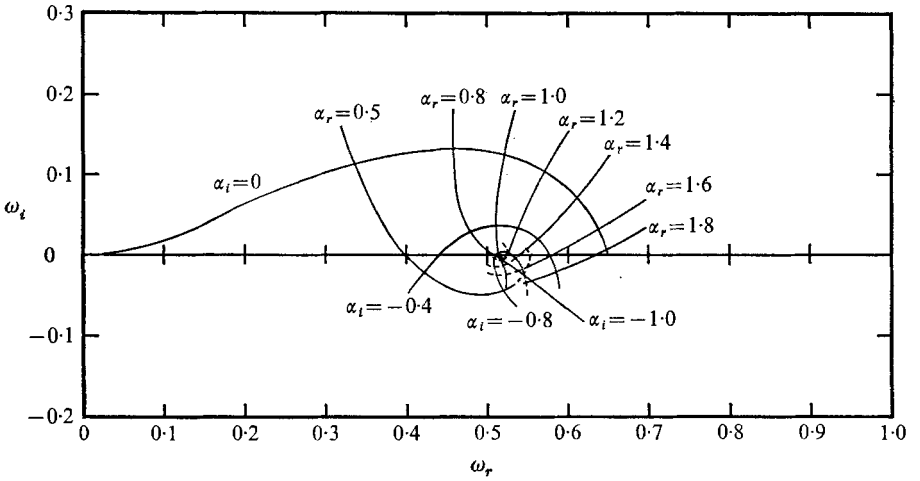

FIGURE 11. Combined stability eigenvalue results: mode I disturbances. $x/L = 0{\cdot}02$.

result of the displacement of the saddle-point, the $\omega_i = 0$ contours pertaining to the upstream- and downstream-moving groups of waves are continuous. Although the relationship $\alpha = \alpha(\omega)$ is not presented, this result can be determined from figures 5 and 7.

Figure 12 presents for mode I disturbances the eigenvalues transformed to the spatial frame using the group velocity. It is found from these results, which are based on the temporal analysis, that disturbances having frequencies

$$0 < \omega_r < 0{\cdot}650$$

and wavenumbers $0 < \alpha_r < 1{\cdot}762$ are unstable with spatial amplification rates in the interval $0 < \alpha_r c_i/U_{\text{group}} < 0{\cdot}470$. Of these disturbances, the one having $\omega_r = 0{\cdot}560$ and a wavenumber $\alpha_r = 1{\cdot}14$ will dominate all others by virtue of its maximum amplification rate, $\alpha_r c_i/U_{\text{group}} = 0{\cdot}470$.

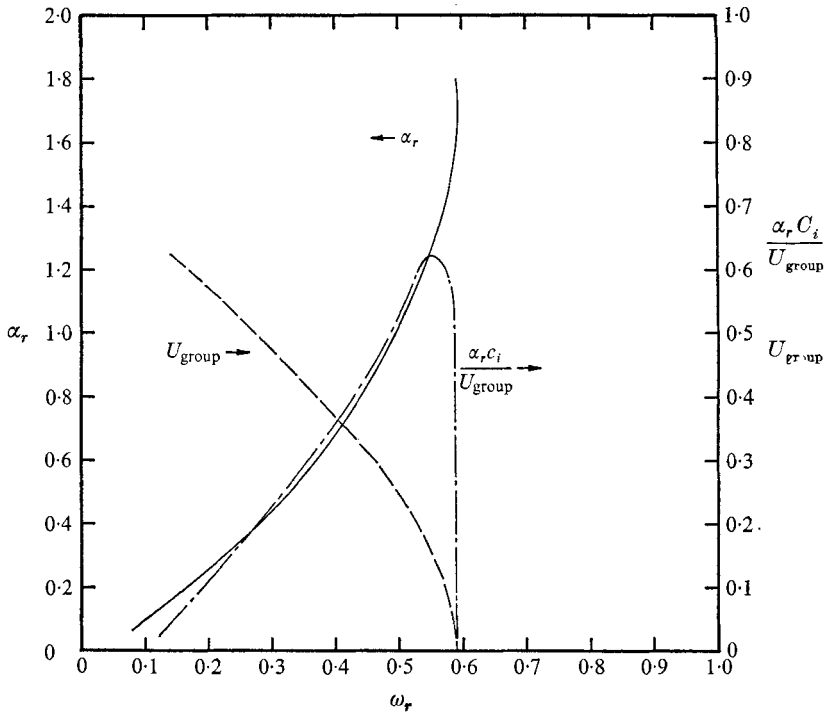

FIGURE 12. Transformed temporal stability eigenvalue results: mode I disturbances. $x/L = 0{\cdot}02$.

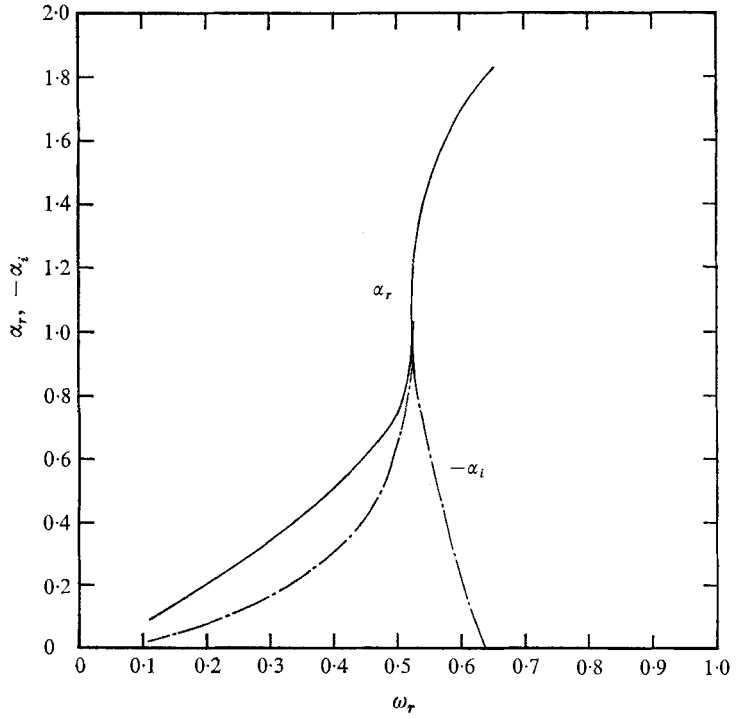

FIGURE 13. Spatial stability eigenvalue results: mode I disturbances. $x/L = 0{\cdot}02$.

The spatial stability eigenvalues, plotted in figure 13, show that disturbances having frequencies in the range $0 < \omega_r < 0{\cdot}650$ and wavenumbers $0 < \alpha_r < 1{\cdot}762$ are predicted to be unstable. These mode I eigenvalue results indicate that the wake profile at $x/L = 0{\cdot}02$ is a highly tuned amplifier for a disturbance frequency of $\omega_r = 0{\cdot}520$ and wavenumber $\alpha_r = 1{\cdot}0$ because of its amplification rate $\alpha_i = -1{\cdot}0$.

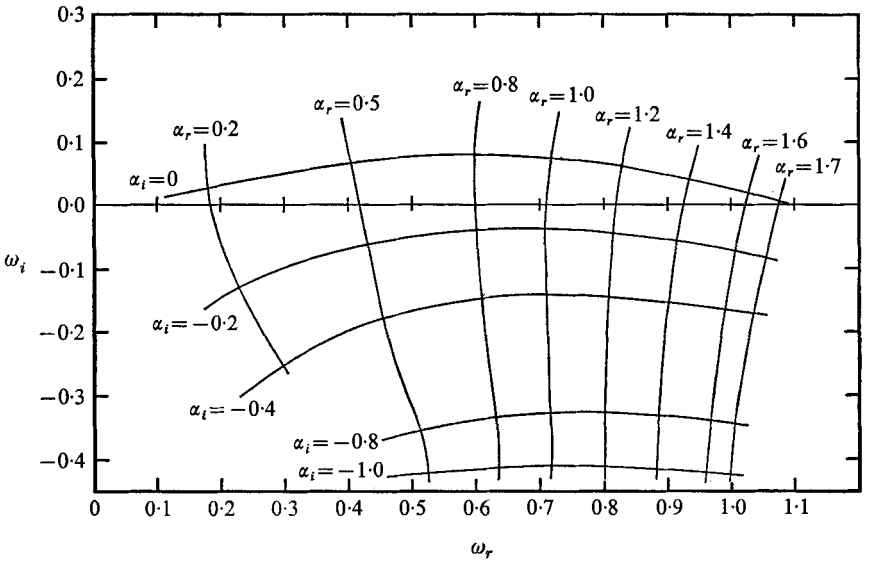

FIGURE 14. Combined stability eigenvalue results: mode I disturbances. $x/L = 0{\cdot}30$.

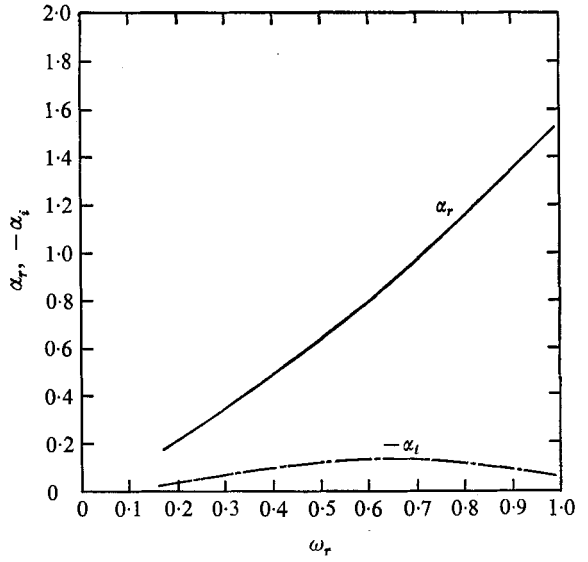

FIGURE 15. Spatial stability eigenvalue results: mode I disturbances. $x/L = 0{\cdot}30$.

Disturbance eigenvalues for wake stations between $x/L = 0{\cdot}02$ and $x/L = 0{\cdot}30$ will be deleted for the sake of brevity, since only slight variations of the previous results are found (see Mattingly (1968) for details). At the final wake station considered, $x/L = 0{\cdot}30$, the wake centre-plane velocity is found to be $U_c = 0{\cdot}440$. The combined stability eigenvalues are plotted in figure 14; those for the spatial reference frame are shown in figure 15. The contours in figure 14 indicate that the saddle point has continued to move even farther below the ω_r axis. In the spatial analysis, the dominant disturbance has $\omega_r = 0{\cdot}650$ and $\alpha_r = 0{\cdot}887$ with amplification rate $\alpha_i = -0{\cdot}130$.

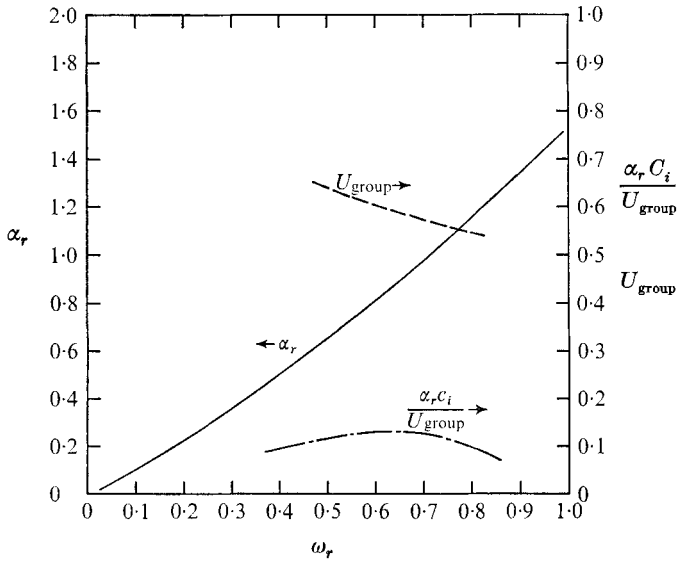

FIGURE 16. Transformed temporal eigenvalue results: mode I disturbances. $x/L = 0{\cdot}30$.

Figure 16 shows the pertinent eigenvalues transformed to spatial results in the temporal framework. By virtue of its maximum amplification rate of

$$\alpha_r c_i / U_{\text{group}} = 0{\cdot}130,$$

the most unstable symmetrical disturbance has frequency $\omega_r = 0{\cdot}650$ and wavenumber $\alpha_r = 0{\cdot}880$. When these transformed temporal results are compared with the corresponding characteristics of the spatial case, they are found to be identical, thereby verifying Gaster's (1963) conclusion regarding the relevance of the group velocity transformation.

The mode II combined stability eigenvalues for wake station $x/L = 0{\cdot}30$ are plotted in figure 17 with the spatial results shown in figure 18. The most unstable disturbance is found to have $\omega_r = 0{\cdot}275$ and $\alpha_r = 0{\cdot}459$ with an amplification rate $\alpha_i = -0{\cdot}034$.

The dominant disturbance characteristics as predicted by the linearized stability theory and based upon the quasi-uniform assumption are listed in tables 1, 2 and 3.

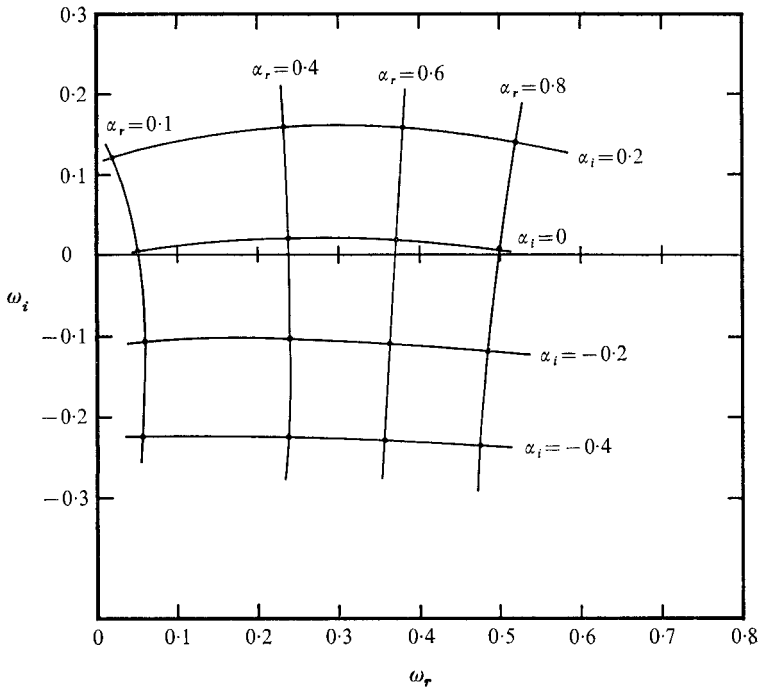

FIGURE 17. Combined stability eigenvalue results: mode II disturbances. $x/L = 0{\cdot}3$.

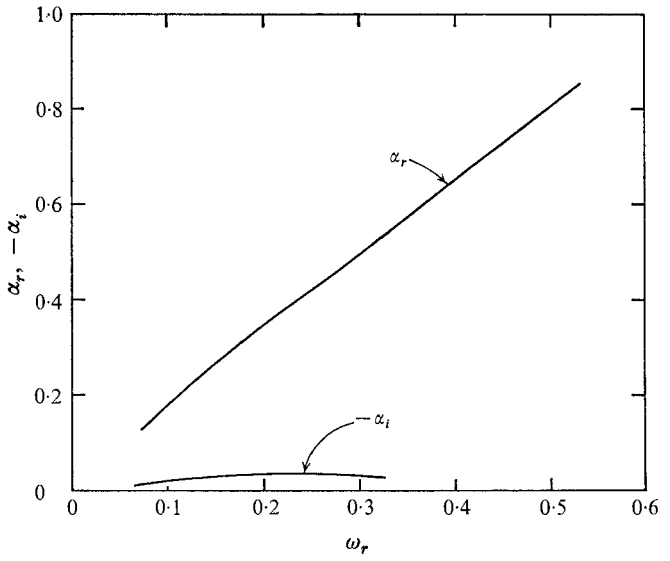

FIGURE 18. Spatial stability eigenvalue results: mode II disturbances. $x/L = 0{\cdot}3$.

For mode I disturbances, the angular frequency at the successive wake stations is observed to increase monotonically with downstream distance in the range $0{\cdot}492 < \omega_r < 0{\cdot}650$. At the same time, the most highly amplified wavenumber is

found to decrease monotonically throughout the interval $1{\cdot}090 > \alpha_r > 0{\cdot}887$. Interesting behaviour is also noted in the longitudinal distribution of the spatial amplification rate. Between $x/L = 0{\cdot}003$ and $x/L = 0{\cdot}02$, the quantity $-\alpha_i$ is found to increase with downstream distance. At $x/L = 0{\cdot}02$ where, it is recalled, the saddle point just passed through the ω_r axis (see figure 11), the spatial amplification rates reaches a maximum value. Past this wake station, the spatial amplification rate of the dominant disturbance at each wake station exhibits a monotonically decreasing dependence with downstream direction.

x/L	0·003	0·02	0·05	0·15	0·30
U_c	0·0012	0·0532	0·1290	0·308	0·440
$-\alpha_i$	0·700	1·000	0·411	0·202	0·130
α_r	1·090	1·000	0·994	0·900	0·887
ω_r	0·492	0·520	0·550	0·600	0·650

Wake profile $U = 1-(1-U_c)\,\mathrm{sech}^2\,\sigma Y$.

TABLE 1. Spatial stability eigenvalues for mode I disturbances

x/L	0·003	0·02	0·05	0·15	0·30
U_c	0·0012	0·0532	0·1290	0·308	0·440
$-\alpha_i$	0·110	0·095	0·078	0·049	0·034
α_r	0·398	0·399	0·406	0·447	0·459
ω_r	0·110	0·125	0·150	0·225	0·275

Wake profile $U = 1-(1-U_c)\,\mathrm{sech}^2\,\sigma Y$.

TABLE 2. Spatial stability eigenvalues for mode II disturbances

x/L	0·003	0·02	0·05	0·15	0·30
U_c	0·0012	0·0532	0·1290	0·308	0·440
$\alpha_r c_i/U_{\text{group}}$	0·625	0·470	0·340	0·185	0·130
α_r	1·300	1·140	1·070	0·990	0·880
ω_r	0·550	0·560	0·585	0·650	0·650

Wake profile $U = 1-(1-U_c)\,\mathrm{sech}^2\,\sigma Y$.

TABLE 3. Temporal stability eigenvalues for most highly amplified mode I disturbances

In table 2, the frequency of the dominant antisymmetrical disturbances at each successive wake station is predicted, according to spatial theory, to increase with downstream distance through the range $0{\cdot}110 < \omega_r < 0{\cdot}275$. The disturbance wavenumber is also found to increase monotonically from $\alpha_r = 0{\cdot}398$ to $\alpha_r = 0{\cdot}459$. It is also noted that the antisymmetrical amplification rates decrease steadily from $-\alpha_i = +0{\cdot}110$ to $\alpha_i = 0{\cdot}034$. Thus, despite the varied dependence of amplification rate upon downstream distance, the present spatial theory demonstrates that mode II disturbances are everywhere dominated by the mode I variety throughout the interval

$$0{\cdot}003 < x/L < 0{\cdot}30.$$

Table 3 lists the characteristics of the dominant mode I disturbances predicted by the temporal analyses where the group velocity transformation is used. It is found that frequency of the most highly amplified eigenmode exhibits a dependence on downstream distance that increases monotonically from 0·550 to 0·650. Although this trend is in agreement with the corresponding results of the spatial theory, the quantitative differences are apparent at the upstream wake stations.

The dominant wavenumber distribution, which according to the temporal viewpoint decreases steadily from $\alpha_r = 1{\cdot}300$ to $\alpha_r = 0{\cdot}880$, agrees qualitatively with the spatial results. Once again, though, the quantitative discrepancies prevail where amplification levels are high. Where spatial growth rates are small, the equivalence of the two viewpoints is apparent.

It is important to note the difference between the downstream distributions of the temporal and spatial results for amplification rate. The temporal prediction, which is observed to decrease monotonically from 0·625 to 0·130, should be contrasted with that of the spatial analysis. Note also the marked qualitative and quantitative differences.

4.4. *Eigenfunction computations*

Knowing the characteristics of the most highly amplified disturbances at the successive wake stations, we now examine distributions of the corresponding eigenfunctions. The longitudinal and transverse disturbance velocities and the disturbance vorticity distributions will be presented only for wake stations $x/L = 0{\cdot}003$, 0·02 and 0·30. These distributions are presented for mode I and II disturbances using the spatial theory and for mode I disturbances using the transformed-temporal theory where the group velocity is used.

Knowing the most highly amplified mode I disturbance characteristics at wake stations $x/L = 0{\cdot}003$, 0·02 and 0·30, the corresponding longitudinal and vertical disturbance velocities are computed. The results, which are plotted in figure 19, show that the longitudinal component of disturbance velocity has basically the same form through this near wake region. Close scrutiny reveals that the maximum amplitude occurs at $Y = 0{\cdot}60$, just inside the critical layer located at $Y = \pm 0{\cdot}75$. Furthermore, this peak amplitude is found to decrease slightly between $x/L = 0{\cdot}003$ and $x/L = 0{\cdot}02$ and to increase between $x/L = 0{\cdot}02$ and $x/L = 0{\cdot}30$, where it reaches a maximum exceeding that at the initial wake station. The amplitude of the transverse disturbance velocity component has the same shape throughout this near wake region with the distribution becoming broader as the downstream distance increases.

The plot of the phase angle $\theta_{\mathbf{v}}(Y)$ indicates the symmetry of the transverse disturbance velocity for all three wake stations. At the edges of the wake, this phase angle approaches π radians, at the downstream location $x/L = 0{\cdot}003$. Farther downstream $\theta_{\mathbf{v}}(Y)$ reaches a phase angle of π radians at $Y = \pm 2{\cdot}6$. However, there is no reversal of the transverse disturbance velocity at this point, or at any downstream station. The distributions of the phase angle $\theta_{\mathbf{u}}(Y)$ for the longitudinal disturbance velocity demonstrate that at each wake profile a phase shift of π radians occurs at $Y = 0$, thereby confirming the distribution of $\mathbf{u}$ to be antisymmetrical.

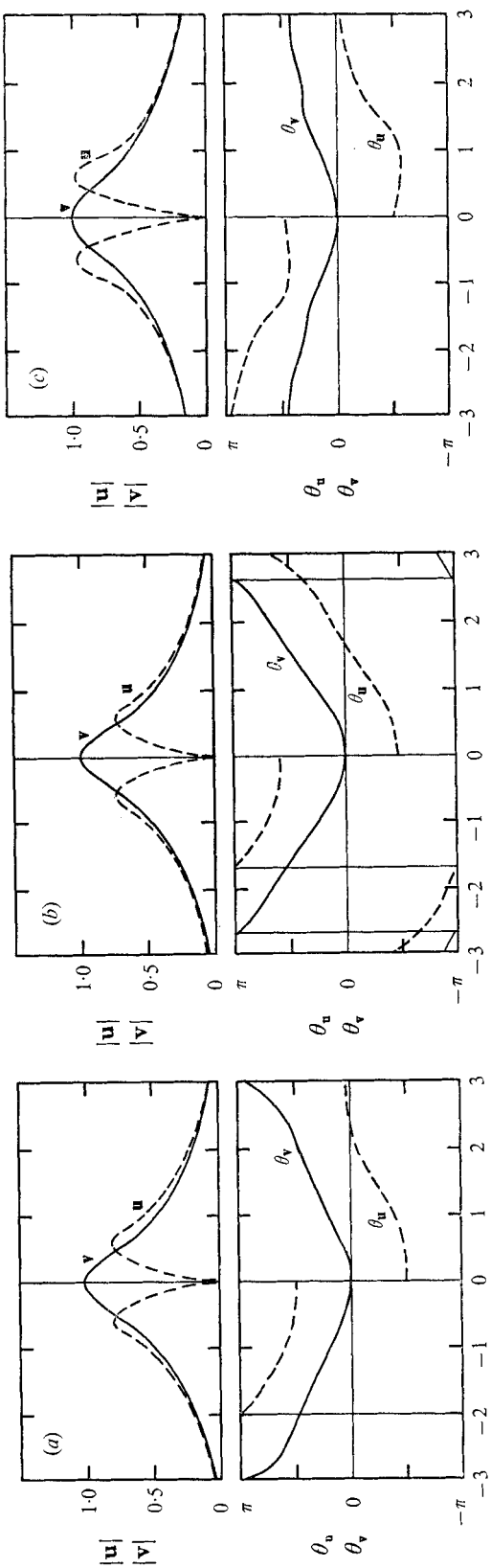

FIGURE 19. Mode I eigenfunctions $\mathbf{u}(Y)$ and $\mathbf{v}(Y)$ with respective phase angles $\theta_u(Y)$ and $\theta_v(Y)$ for three wake stations.
(*a*) $x/L = 0{\cdot}003$, (*b*) $x/L = 0{\cdot}02$, (*c*) $x/L = 0{\cdot}03$.

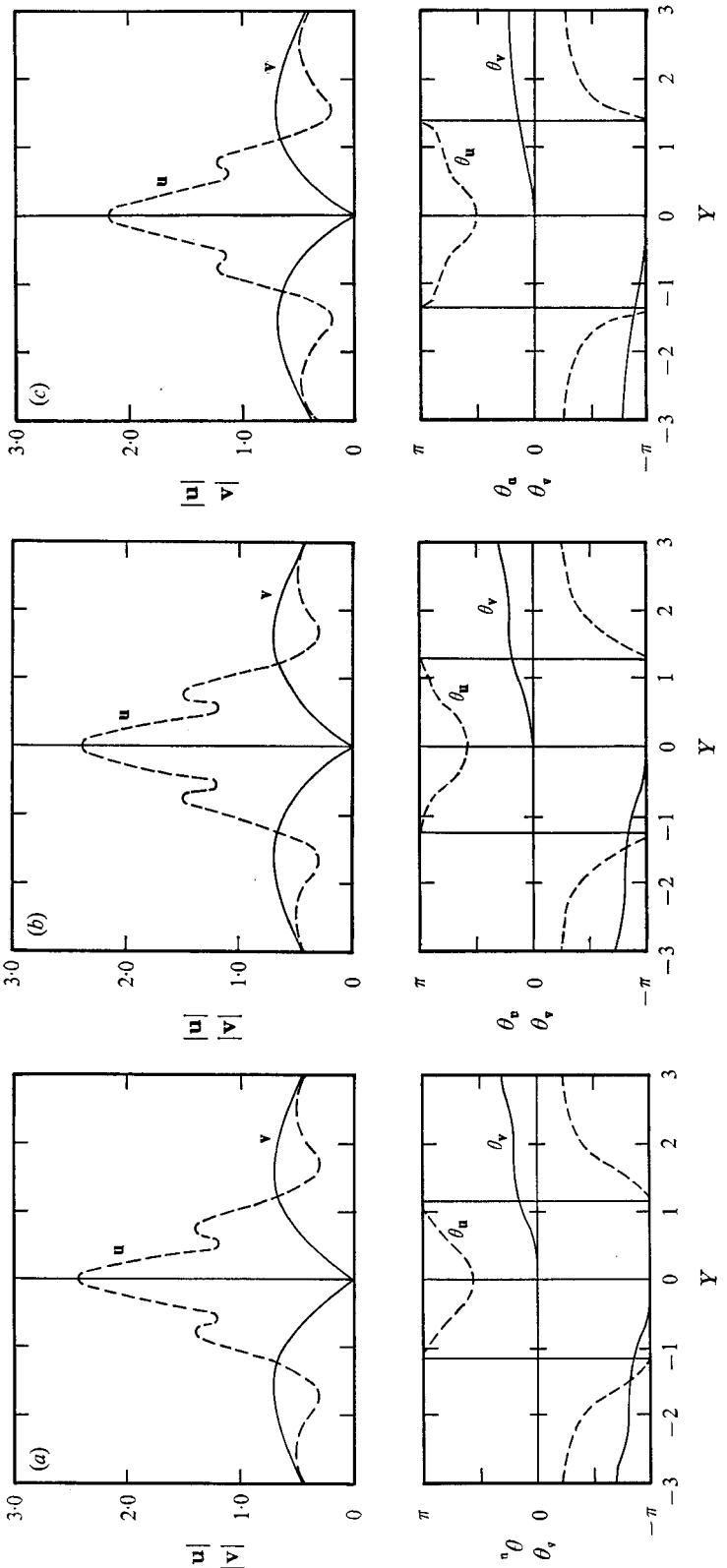

FIGURE 20. Mode II eigenfunctions $\mathbf{u}(Y)$ and $\mathbf{v}(Y)$ with respective phase angles $\theta_u(Y)$ and $\theta_v(Y)$ for three wake stations.
(*a*) $x/L = 0{\cdot}003$, (*b*) $x/L = 0{\cdot}02$, (*c*) $x/L = 0{\cdot}3$.

The most highly amplified mode II disturbance characteristics from wake stations $x/L = 0{\cdot}003$, $0{\cdot}02$ and $0{\cdot}30$ enable computation of the corresponding eigenfunctions. Longitudinal and transverse disturbance velocities are presented in figure 20. Note that the amplitudes $\mathbf{u}(Y)$ and $\mathbf{v}(Y)$ have essentially the same form throughout this near wake region. Furthermore, the minor peaks in the $\mathbf{u}(Y)$ distribution increase between the initial profile and wake station $x/L = 0{\cdot}02$. Between this wake station and $x/L = 0{\cdot}30$, these same peaks decrease. The transverse component amplitude exhibits a cross-stream profile that remains unchanged qualitatively with downstream distance between $x/L = 0{\cdot}003$ and $x/L = 0{\cdot}30$.

The phase diagrams also remain essentially unchanged throughout this wake region. With the zero amplitude at the wake centre-plane and a shift of π radians at this location, the transverse component of the disturbance velocity continuously reverses directions. As the distribution $\theta_{\mathbf{u}}(Y)$ is continuous in the cross-stream direction and symmetric with respect to $Y = 0$, we conclude that the velocity $\mathbf{u}$ is also symmetric. We thereby verify the antisymmetric character of mode II disturbances.

Figure 21 (*a*) presents the results of cross-stream distributions of vorticity for mode I disturbances. Three vorticity peaks are found at each of the wake stations, with the largest occurring on the centre-plane in accordance with the mean profile curvature. Note that the vorticity changes sign as the mean profile curvature changes sign at the critical layer. The secondary peaks in vorticity occur outside the critical layer at the two upstream wake stations at $Y = \pm 1{\cdot}0$. In the downstream co-ordinate, these secondary peaks exhibit a decrease in amplitude between the two upstream wake stations. Between the two downstream wake stations, these secondary peaks are found to increase markedly, reaching an amplitude of more than twice the corresponding value at the initial profile. In addition, the transverse location of the secondary vorticity peaks increases slightly at the downstream profile. The distribution of disturbance vorticity in this near wake region suggests a new vortex street generation process. The new mechanism will be presented in the following discussion as an alternative to that put forth by Sato & Kuriki (1961).

The mode II vorticity distributions are presented in figure 21 (*b*). Two major peaks occur, plus an additional phase shift due to the antisymmetric character of $\mathbf{v}(Y)$. The secondary peaks remain essentially unchanged while the major peaks diminish with downstream distance.

Proceeding toward the formation of the von Kármán vortex street, which is ultimately developed in the wake of flat plates and thin airfoils, we now consider the Sato & Kuriki vortex model. They speculate that near the trailing edge of the wake generating body, a single row of vortices, which rotate alternatively in opposite directions, lies along the centre-line of the wake. This model accounts for their anemometer data in this region of the wake. At some point farther downstream, alternate vortices are displaced transversely in accord with the local-induced velocity fields, and a vortex street is thereby formed. The vortex street configuration is found to be stable until three-dimensional distortional effects ultimately cause the wake to become turbulent.

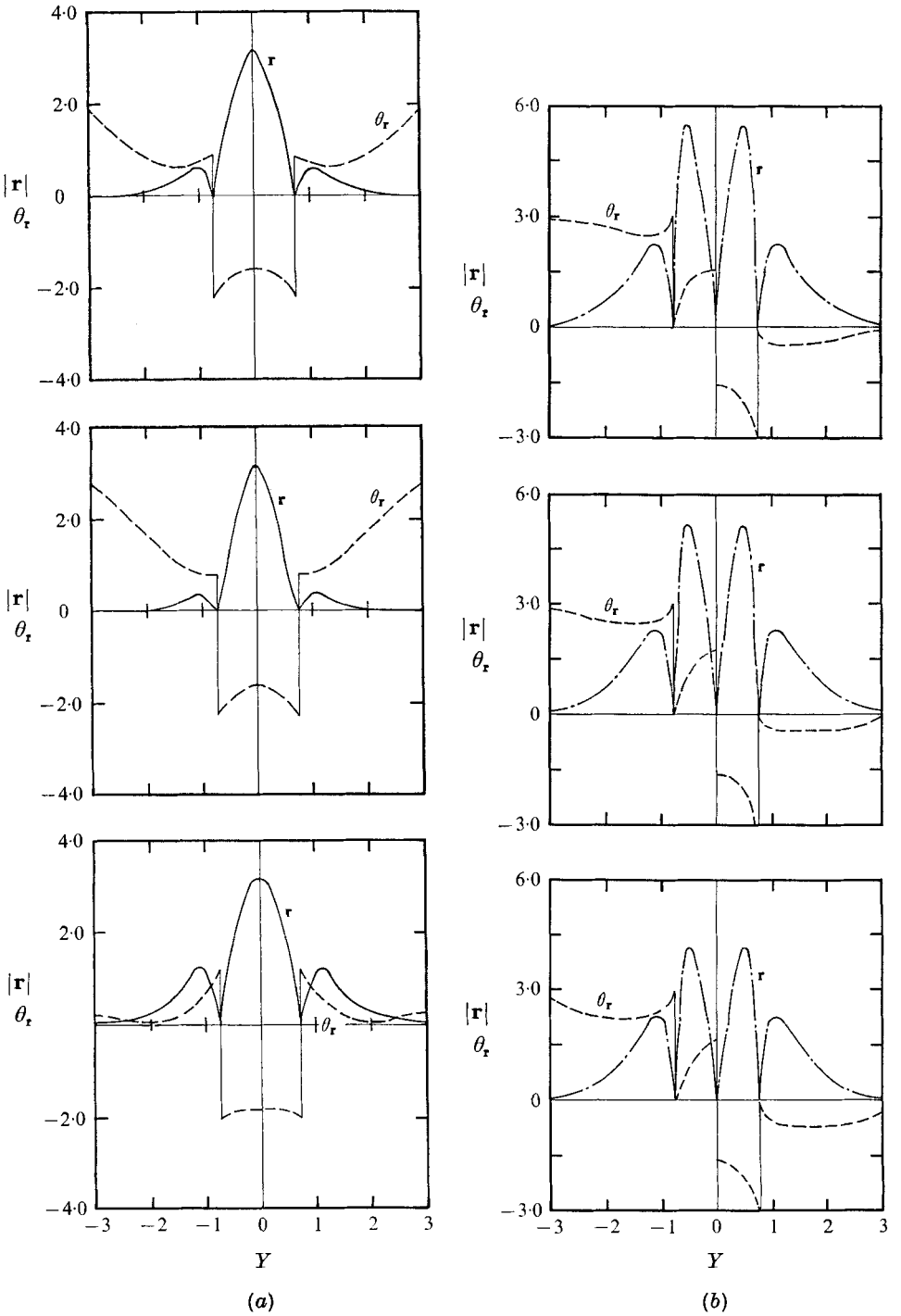

FIGURE 21. Distribution of disturbance vorticity, $\mathbf{r}(Y)$ and phase angle $\theta_{\mathbf{r}}(Y)$ at three wake stations. (*a*) Mode I disturbances. (*b*) Mode II disturbances. Top to bottom: $x/L = 0{\cdot}003$, $x/L = 0{\cdot}02$, $x/L = 0{\cdot}3$.

The present model is suggested in contrast to that of Sato & Kuriki. According to the linearized stability theory, the disturbance vorticity distributions presented in figure 21(*a*) are superposed on the mean vorticity of the respective wake velocity profiles. It is recalled that all the eigenfunction distributions are scaled relative to the symmetry conditions imposed at $Y = 0$ and that exponential amplification factors are temporarily excluded.

When the mode I vorticity distributions are superposed upon the mean values, it is found that at $Y = 0$ the only vorticity component present is that of the disturbance. This vorticity component is the major peak shown in each of the cross-stream profiles in figure 21(*a*). In addition, the secondary vorticity peaks that occur beyond the critical layers are also superposed upon their respective mean vorticity profiles. Here, the mean vorticity, being antisymmetric with respect to $Y = 0$, is not zero and is oppositely signed. Therefore, the superposition produces a vorticity component at $Y = 0$ that oscillates about the zero mean vorticity.

Just beyond the critical layers, two other oscillating components occur that are in phase with each other. Each of these components, it is recalled, is out of phase with the centre-line component. Consequently, these two secondary vorticity peaks produce an additive contribution to the mean vorticity beyond one of the critical layers and a subtractive contribution beyond the other. Half a cycle later, the situation is reversed. Where the superposition was additive, it becomes subtractive and vice versa. It has been shown from the disturbance vorticity distribution that these secondary vorticity peaks are reduced with downstream distance between wake station $x/L = 0{\cdot}003$ and $0{\cdot}02$. However, between $x/L = 0{\cdot}02$ and $0{\cdot}30$, these same peaks are found to increase markedly to amplitudes that exceed twice their values at the initial wake station. As a result, oppositely signed vorticity concentrations would be highly amplified on either side of the wake centre-plane. These oppositely signed vorticity concentrations would be displaced in time according to the disturbance frequency. On the wake centre-plane, the oscillating disturbance vorticity component is again amplified, but at a reduced spatial rate.

It is therefore concluded that although an amplified and oscillating component of disturbance vorticity exists on the wake centre-plane, vorticity concentrations located beyond the critical layers are even more highly amplified. The concentrations are predicted, according to the linearized spatial stability theory, to have the longitudinal spacing and the proper phase relationships that pertain to the classic von Kármán street.

As a result, in contrast to the mechanism proposed by Sato & Kuriki, the vortex street development does in fact, begin in the very near wake and in accord with the predictions of the linearized theory. As the disturbance quantities are amplified in the more distant wake, the previously neglected non-linear terms in the equations of motion undoubtedly are needed to describe the vortex street phenomena. As the double row vortex street configuration is developed further, the anemometer response in the wake centre-plane region indicates the second harmonic component as seen in the fluctuation map of figure 2.

In addition to the distributions of disturbance velocities and vorticity, the

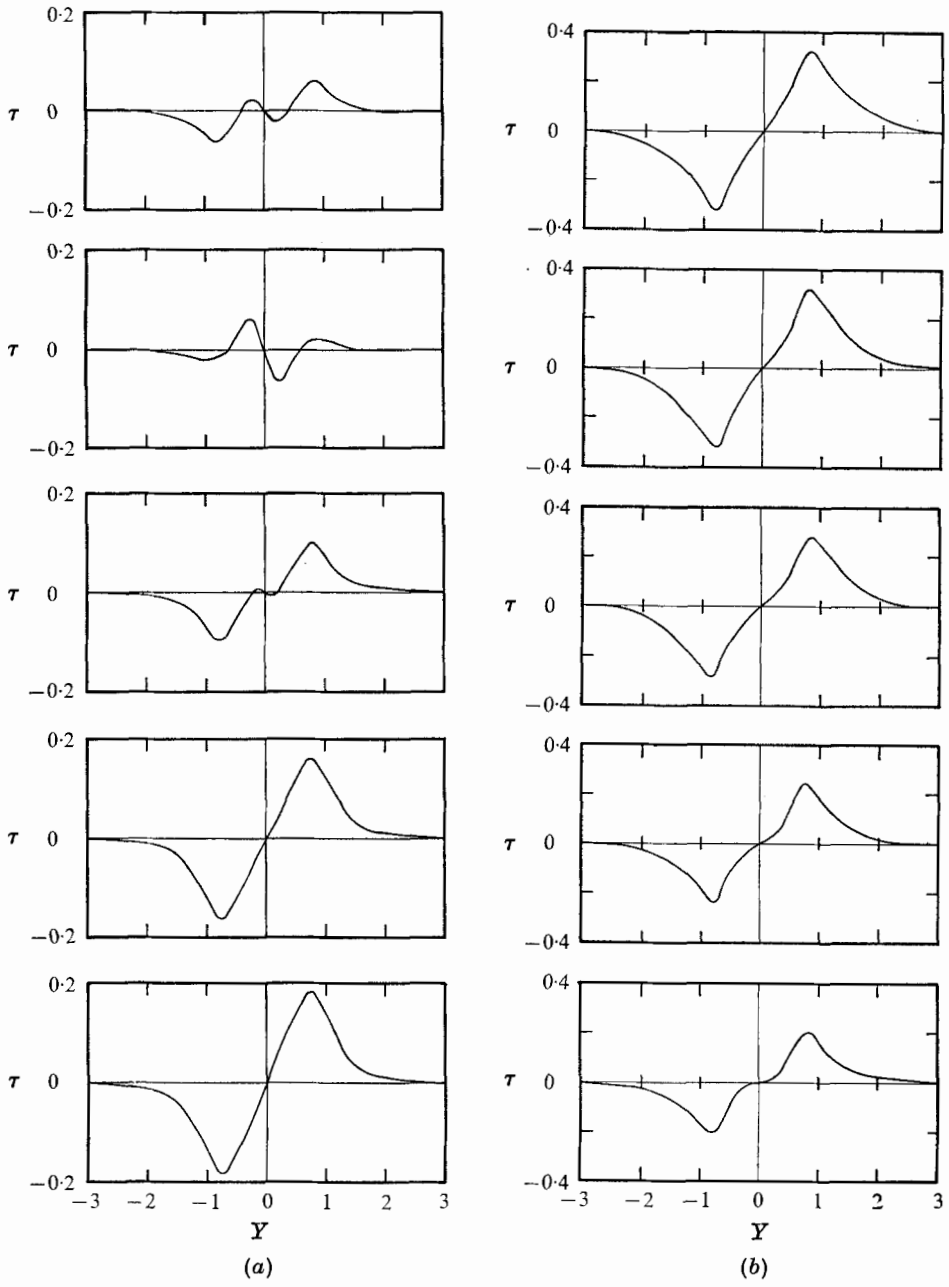

FIGURE 22. Reynolds stress distributions at five wake stations according to spatial theory. (*a*) Mode I disturbances. (*b*) Mode II disturbances. Top to bottom: $x/L = 0{\cdot}003$, $x/L = 0{\cdot}02$, $x/L = 0{\cdot}05$, $x/L = 0{\cdot}15$, $x/L = 0{\cdot}03$.

Reynolds stress profiles were calculated. These stresses provide the mechanism through which energy from the mean flow is transferred to the disturbance motion. When the local Reynolds stress (defined in equation (3.15)) and the mean vorticity are of like sign, the disturbance energy increases at the expense of the

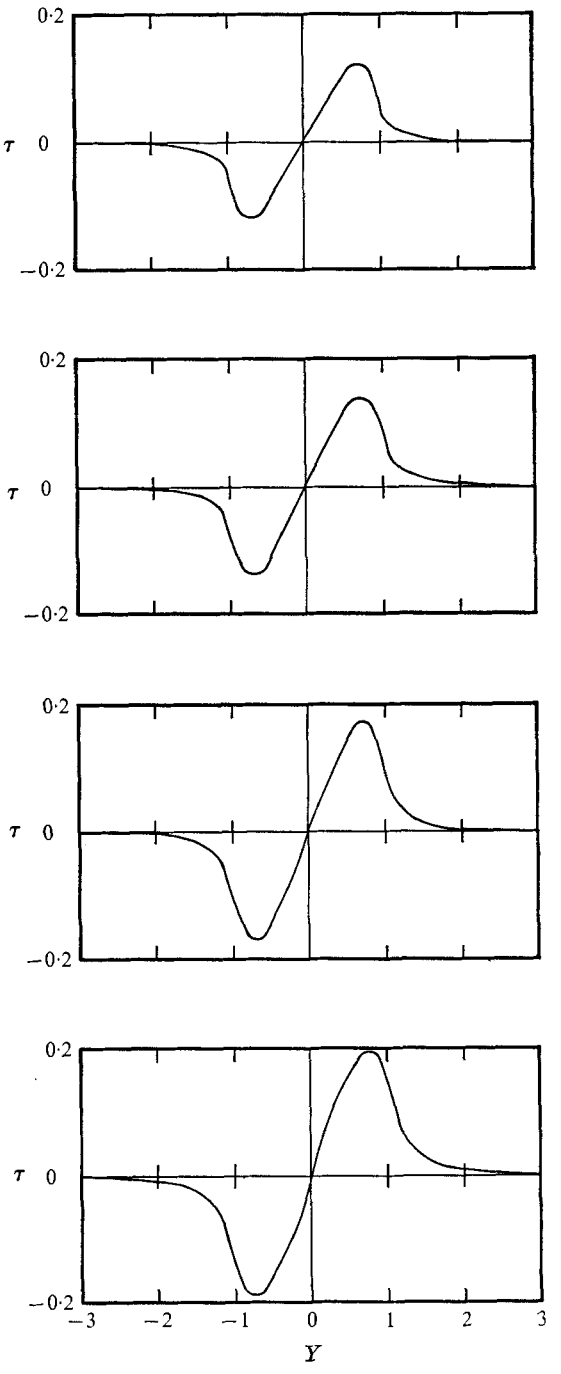

FIGURE 23. Distribution of the Reynolds stress, τ at successive wake stations. Transformed temporal theory. Mode I disturbance. Top to bottom: $x/L = 0{\cdot}003$, $x/L = 0{\cdot}02$, $x/L = 0{\cdot}5$, $x/L = 0{\cdot}15$.

mean motion. Conversely, Reynolds stress and mean vorticity of opposite sign imply energy transfer from the disturbance to the mean motion.

The Reynolds stress distributions were calculated for the most highly amplified of both mode I and II disturbances according to the spatial theory. In addition, there are presented the Reynolds stress distributions for the most highly amplified mode I disturbances at successive wake stations according to the temporal theory where the group velocity transformation is used to convert to the spatial reference frame.

The Reynolds stress distributions for the spatial stability predictions of the most highly amplified mode I disturbances are presented in figure 22 (*a*). Throughout the five wake stations, the Reynolds stress is appropriately antisymmetric with respect to $Y = 0$. It is important to note the variation of the cross-stream distributions with downstream distance. At the initial wake station, the Reynolds stress and the mean vorticity are of opposite sign on either side of and adjacent to the wake centre-plane. In this region, energy is transferred from the disturbance to the mean motion. This transfer of energy to the mean motion near $Y = 0$ is continued at wake station $x/L = 0{\cdot}02$ where the Reynolds stress reaches a stabilizing peak at $Y = \pm 0{\cdot}25$. With farther distance downstream, this stabilizing Reynolds stress changes continuously into a completely destabilizing cross-stream profile at $x/L = 0{\cdot}15$ and $0{\cdot}30$.

In figure 22 (*b*), the Reynolds stress distributions are presented for the most highly amplified mode II disturbance characteristics. The qualitative aspects of the cross-stream distributions are essentially preserved throughout the five wake stations. Figure 23 presents the cross-stream Reynolds stress distributions for the most highly amplified mode I disturbances predicted with the temporal analysis where the group velocity transformation is used to obtain spatial results. A comparison of this distribution with those of the true spatial analysis reveals both qualitative and quantitative discrepancies. It is concluded, therefore that only the complex wavenumber model should be used to perform the stability analyses at the successive wake stations.

5. Measurement of disturbance characteristics

Using anemometry, measurements at successive wake stations were made of the disturbance wavelength, frequency, and the r.m.s. distributions for the longitudinal component of the disturbance velocity. Measurements of the longitudinal r.m.s. velocity also provided a determination of the symmetry characteristics of the natural disturbances occurring in the wake and local values of the spatial amplification rate.

Experimental results for the disturbance frequency were obtained from anemometer oscillographs (see figure 2). Because this figure shows the disturbance amplitudes to be maximum just off the wake centre-plane, the frequency survey was conducted at $Y = 1{\cdot}0$.

The cross-stream distributions of $\tilde{u}^2/U_\infty$ for successive wake stations in the near wake region are presented in figure 24. The maximum values of these distributions at each location were reproducible to the extent shown by the

multiple data points. Although phase measurements were not made for the longitudinal disturbance velocities on either side of the wake centre-plane, these results are to be compared with the corresponding eigenfunctions for mode I and mode II disturbances. The qualitative results confirm that the naturally amplifying disturbances in the wake are of the mode I variety. Local average values of the spatial amplification rate can be obtained from the data presented in figure 24. Using a finite-differencing calculation of the form

$$-\alpha_i = \Delta \log ((\overline{\tilde{u}^2})^{\frac{1}{2}}/U_\infty)/\Delta x$$

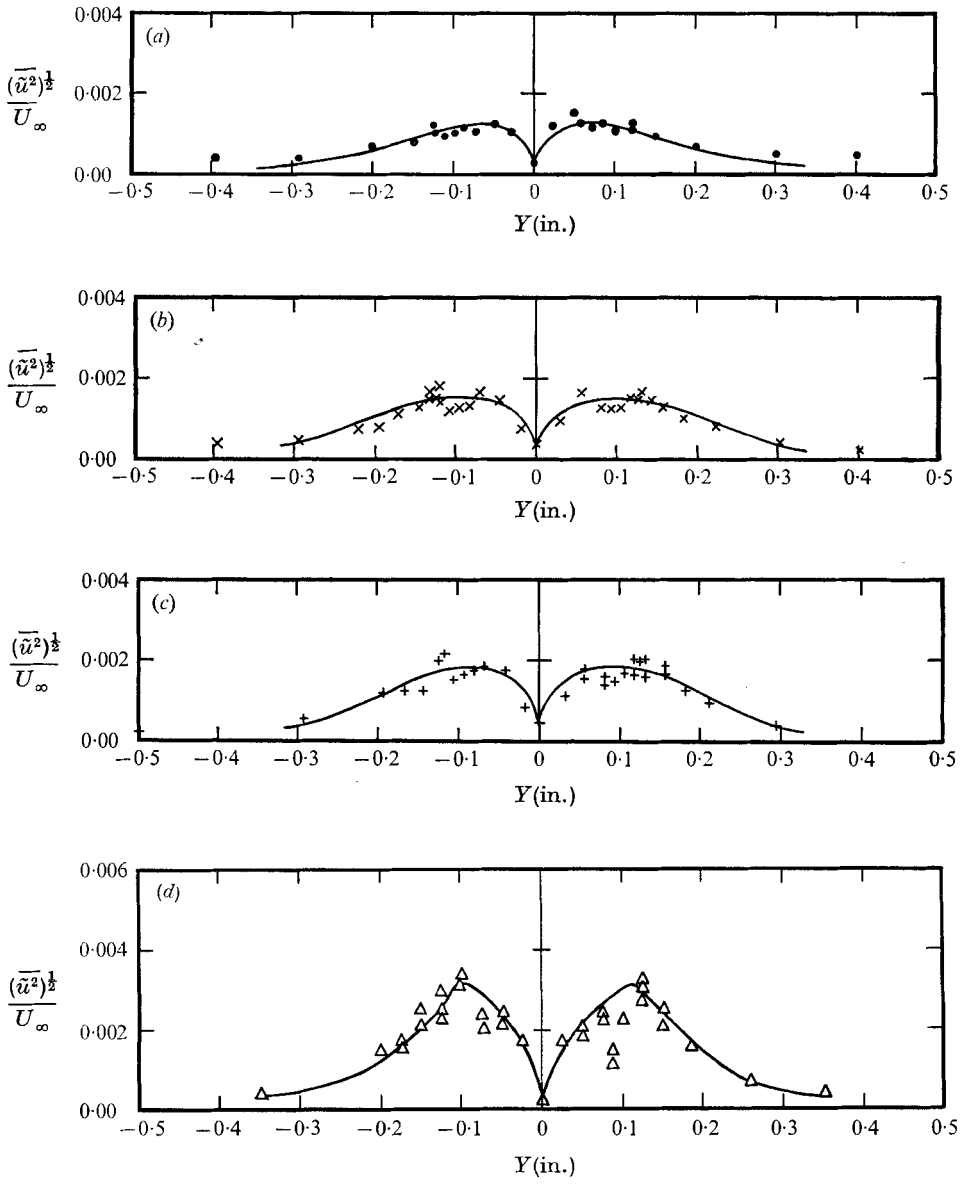

FIGURE 24. For legend see facing page.

applied to the peaks of successive $(\overline{\tilde{u}^2})^{\frac{1}{2}}/U_\infty$ profiles enables determination of $-\alpha_i$ halfway between the profiles.

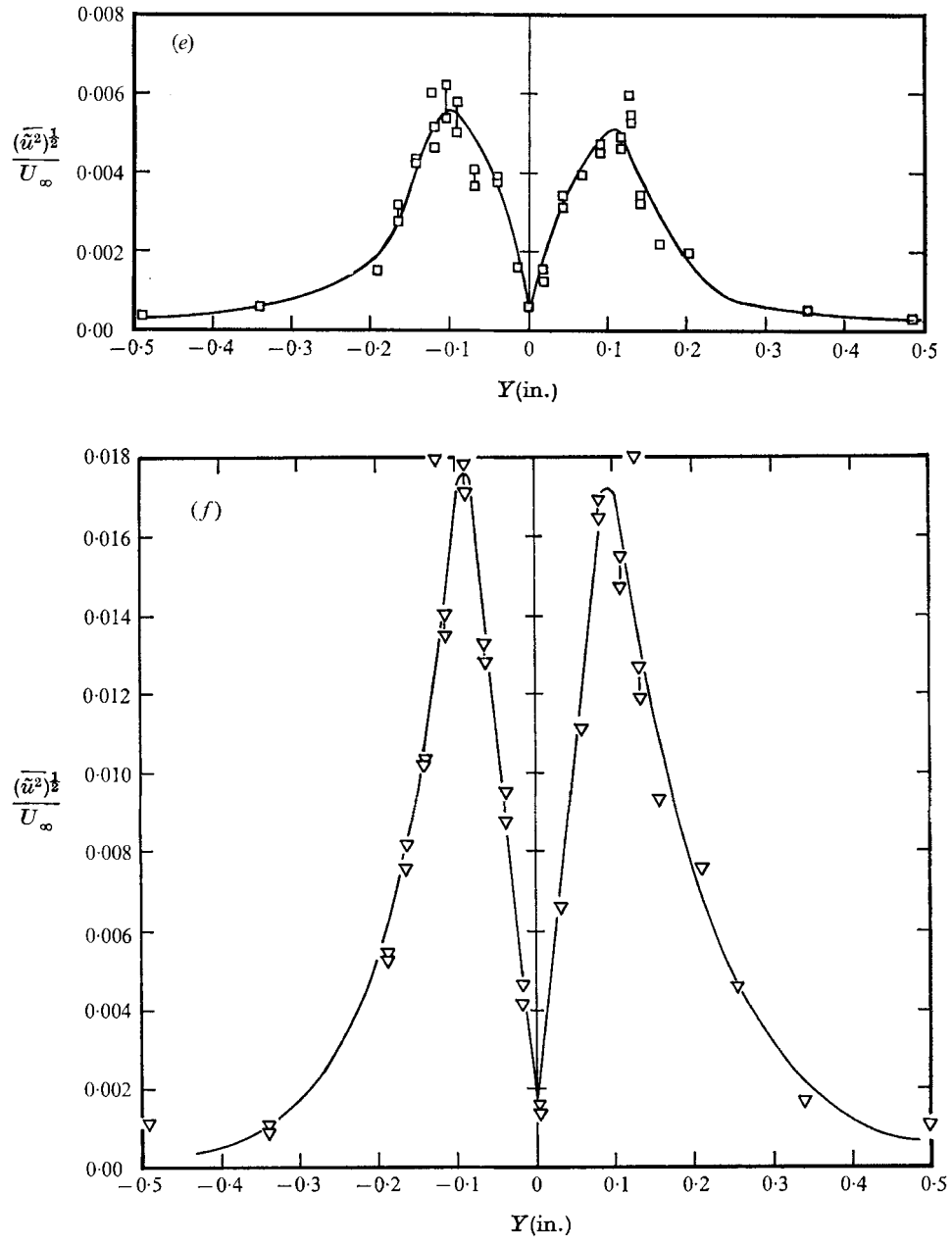

FIGURE 24. Distribution of $(\overline{\tilde{u}^2})^{\frac{1}{2}}/U_\infty$. (*a*) $x/L = 0{\cdot}003$, (*b*) $x/L = 0{\cdot}015$, (*c*) $x/L = 0{\cdot}025$, (*d*) $x/L = 0{\cdot}050$, (*e*) $x/L = 0{\cdot}10$, (*f*) $x/L = 0{\cdot}20$.

6. Comparison of experimentally determined disturbance characteristic with the results of the linear theory

In figure 25, the wavenumber, frequency, and spatial amplification rate are compared with the dominant disturbance characteristics predicted by the spatial theory for mode I disturbances. Qualitative agreement exists between the experimental measurements and the predictions of the linearized spatial stability theory, but quantitative differences are revealed in the wavenumber distributions. The experimentally determined wavenumbers are smaller than those predicted by the inviscid theory.

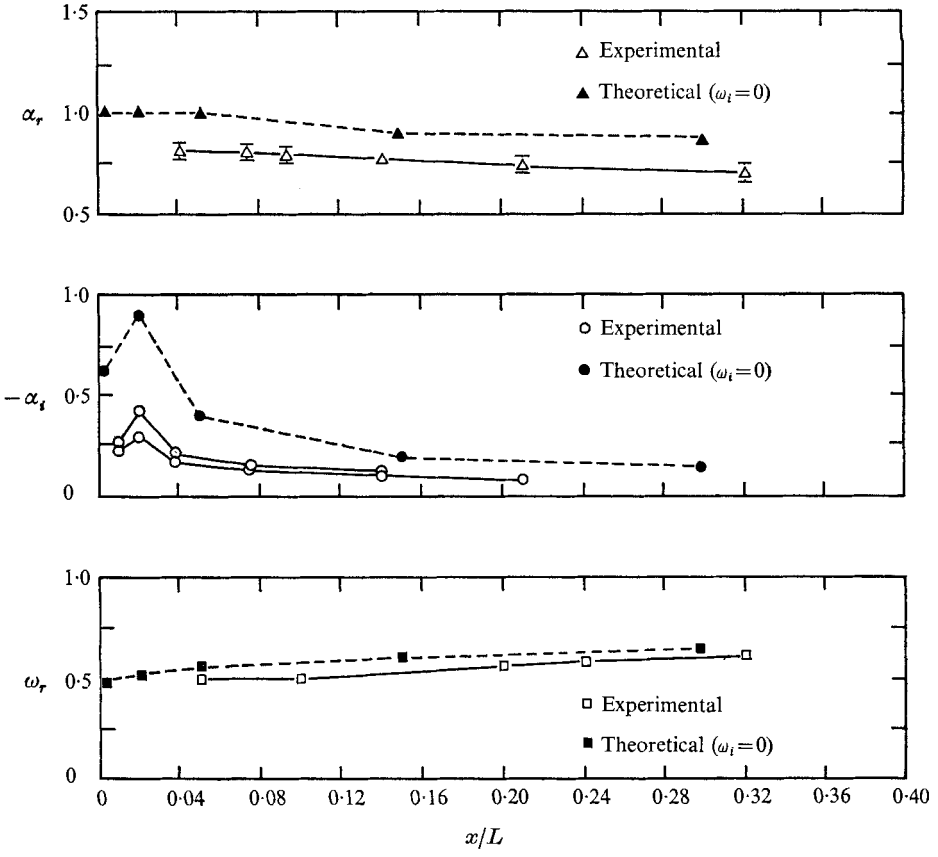

FIGURE 25. Comparison of experimental distributions of disturbance wavenumber, amplification rate, and regular frequency with results of spatial theory.

From the transverse distributions of $\tilde{u}^2/U_\infty$ described earlier, local average values of spatial amplification rate can be found using the finite-differencing method. Results of this calculation are shown in figure 25. Once again, the qualitative agreement in the distributions is considered quite good, while quantitative differences remain between experimental and theoretical results. When the survey was performed again to determine the reproducibility of this distribution, the individual values of spatial amplification rate were found to be

smaller than those of the initial survey, while the qualitative agreement was duplicated. Note that the experimentally determined values are consistently lower than the results of the inviscid theory.

The comparison for the disturbance frequency are presented in figure 25. Although a slight quantitative difference is again noted, with the experimental values being slightly smaller than the corresponding theoretical values, both qualitative and quantitative agreement between the two distributions is considered very good.

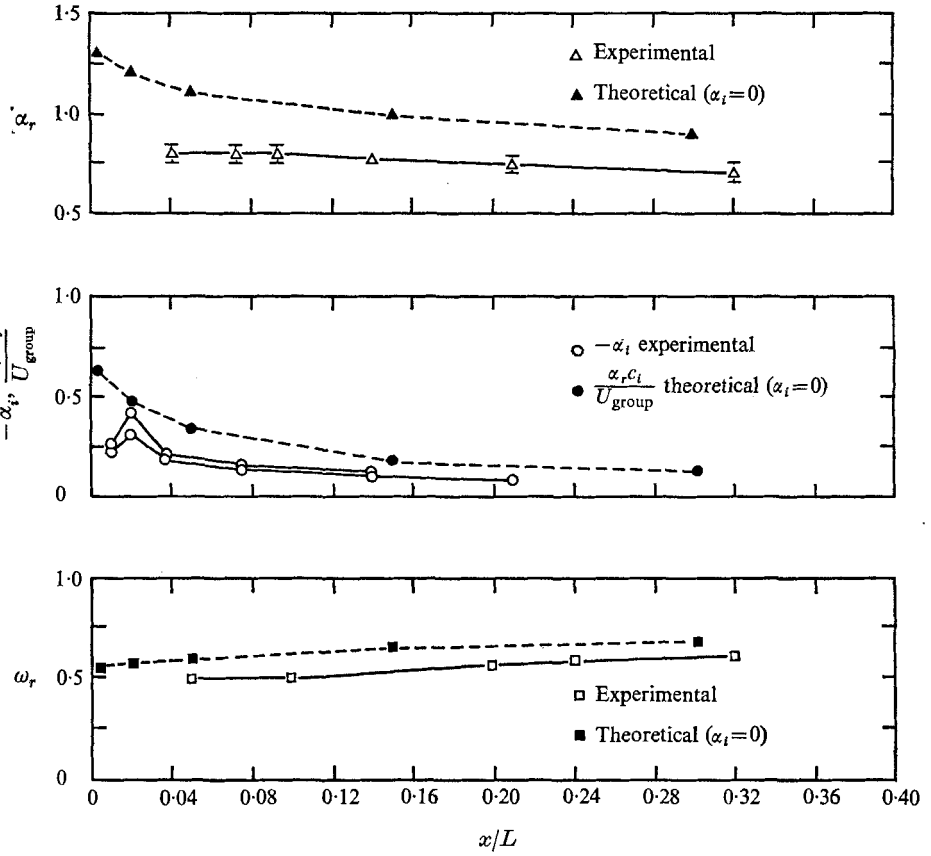

FIGURE 26. Comparison of experimental distributions of disturbance wavenumber, amplification rate, and angular frequency with the transformed results of the temporal theory.

The quantitative discrepancies, which may be attributed to the inviscid assumption, may also be due to the neglected longitudinal gradients in the mean-wake profiles. As previously described, the instability in a free boundary layer for large Reynolds number is essentially inviscid where viscosity has only a damping influence. The stability analysis of Betchov & Szewczyk (1963), which was performed from the temporal viewpoint, showed that inviscid wavenumbers and amplification rates exceed their viscous counterparts and thereby cause quantitative discrepancies. On the other hand, since qualitative agreement

between the results has already been demonstrated, the quantitative aspects of the comparison could probably be improved by incorporating the effects of the local longitudinal gradients in the mean-wake profile.

A comparison of the experimental distribution of disturbance characteristics with the results of the temporal stability theory is shown in figure 26. The temporal amplification rate has been transformed to a spatial one using the group velocity. The wavenumber distributions indicate qualitative agreement between theoretical and experimental values and quantitative differences, with one exception at wake station $x/L = 0{\cdot}3$, where the spatial and temporal analyses predict identical characteristics for the dominant eigenmode.

The comparison of the longitudinal distributions for spatial amplification rates $-\alpha_i$ and $\alpha_r c_i/U_{\text{group}}$ shows that a distinct qualitative difference exists between these two results in the near wake. Farther downstream the agreement between the two distributions corresponds to that observed in figure 25.

The theoretical and experimental distributions for the disturbance angular frequency indicate qualitative agreement between the two results. Again with the exception of wake station $x/L = 0{\cdot}3$, the quantitative differences exceed those noted in figure 25.

It seems reasonable to conclude that the predictions of the spatial theory agree with the experimentally determined disturbance quantities, and that this agreement is both qualitatively and quantitatively superior to the results of the temporal theory. Especially in the near wake, this agreement can be attributed to the large values of ω_i, which are found along the temporal stability line and occur in conjunction with the position of the saddle point in the $\omega = \omega(\alpha)$ and $\alpha = \alpha(\omega)$ planes. When this saddle point lies between the $\alpha_i = 0$ and the $\omega_i = 0$ contours in the $\omega = \omega(\alpha)$ plane, the transformation between these contours via the group velocity is improper and leads to results that differ markedly from the results of the spatial theory.

The analysis of successive downstream wake profiles shows that as the saddle point is displaced from the region between the $\alpha_i = 0$ and the $\omega_i = 0$ contours, the accuracy of the group velocity transformation is improved. Finally, for wake station $x/L = 0{\cdot}3$, the results of the temporal and spatial viewpoints are identical.

Gaster & Davey (1968) found that the temporal and spatial predictions are quite similar when based upon a single Gaussian wake profile comparable to that found in the present work at $x/L = 0{\cdot}15$. They therefore concluded that either viewpoint appears capable of predicting the dominant disturbance characteristics. In light of the present work, this conclusion must be qualified: only profiles beyond wake station $x/L = 0{\cdot}15$ conform to such predictions.

An attempt was made to measure the cross-stream distribution of Reynolds stress. However, the attempt was unsuccessful owing to the infinitesimal size of the velocity fluctuations in this very near wake region.

7. Discussion and conclusions

The inviscid linearized stability theory has been used to analyse the growth of disturbances in the two-dimensional wake of a thin airfoil. The analyses have been made from temporal, spatial and combined viewpoints.

In the near wake region where the linearized analysis is applicable, the mean-velocity profile changes continuously at successive locations. In order to account for the changes, a quasi-uniform approximation is made. By this approximation, successive wake profiles are considered individually and each is taken to be dependent solely upon the transverse co-ordinate. The collective results of the successive stability analyses are then compared with the corresponding disturbance characteristics determined experimentally.

According to the theory, the disturbance predicted to have the maximum spatial amplification rate will dominate all other disturbances for each wake profile considered. With the stability analysis performed both from the temporal and the spatial viewpoints, the relationship between the two frames of reference has been shown. Because the system of unstable waves is shown to be a dispersive one, the conventional transformation scheme using the disturbance phase velocity is clearly incorrect. It is found, however, that there is a proper transformation that relates the two results. This is shown through the results of the combined stability analysis, which demonstrates that disturbance wave-numbers and frequencies predicted to be temporally unstable are also found to be spatially unstable. This transformation is found to be a complicated one in the very near wake because of the location of a saddle point in the eigenvalue planes. The analysis demonstrates that only for certain wake profiles is the transformation from the temporal to spatial framework adequately performed using the group velocity. Using the quasi-uniform approximation, however, the group velocity transformation applied to the dominant disturbance characteristics of the temporal theory renders eigenfunction distributions that are radically different from those of the spatial analysis in the very near wake. The group velocity transformation between the temporal and spatial viewpoints is thereby discarded.

In view of the complexity of the relationship between temporal and spatial viewpoints caused by the saddle-point position, it is concluded that the wake stability analysis must be done solely from the spatial viewpoint. This is verified by comparison of the results of the spatial analysis with experimental measurements of the characteristics of natural disturbances in the wake.

Both symmetrical and asymmetrical disturbances are considered in the present theory. Mode I disturbances (symmetrical in $\mathbf{v}$) effect an oscillation of the mean-wake centre-plane velocity that is transverse to this wake centre-plane. On the other hand, the mode II disturbances (asymmetrical in $\mathbf{v}$), which experience a considerably reduced amplification compared to mode I disturbances and are thereby smothered in the combined superposition of disturbances, cause a longitudinal oscillation of the wake centre-plane velocity.

The eigenvalue results of the spatial stability analysis show that the near wake region behaves like a highly tuned amplifier for mode I disturbances in a

narrow band of angular frequencies. Further, at the initial wake profile, the least damped waves having negative group velocities are found to have disturbances characteristics that coincide exactly with the most highly amplified waves having positive group velocities. With these least damped upstream-travelling groups of waves stimulating the most highly amplified downstream-moving groups of waves, the wake is found to be self-destabilizing. In the downstream wake, the angular frequency of the most highly amplified eigenmode increases slightly. This shift in the angular frequency is accompanied by a reduction in the spatial amplification rate and a slight decrease in the wavenumber of the dominant disturbance. Averaging over the wake region investigated, the wave receiving maximum spatial amplification is the one for which $\omega_r = 0{\cdot}550$ and $\alpha_r = 0{\cdot}994$.

Experimental results are obtained for disturbances that develop *naturally* in an actual wake whose successive wake profiles conform to those used in the linearized stability analyses. Comparison of the experimental disturbance characteristics with the predictions of the linearized spatial stability theory indicates that, while quantitative differences do occur, there is consistent qualitative agreement throughout the wake region investigated. Specifically, mode I disturbances, which are those most highly amplified according to the linearized spatial analysis, are found to occur in the actual wake. Furthermore, whereas the experimentally determined disturbance characteristics exhibit qualitative agreement with the linearized spatial stability theory, they are also seen to differ qualitatively with the linearized temporal stability predictions when these are transformed to spatial values using the group velocity. It is thereby confirmed that the temporal viewpoint where spatial results are achieved by use of the group velocity transformation must be discarded.

Since the consistent quantitative differences still remain between the experimental and theoretical disturbance characteristics, it is felt that future stability investigations include the effect of viscosity. In addition, the neglect of the local longitudinal gradients in the mean-wake flow might be also responsible for the quantitative discrepancies between the experimental and theoretical disturbance characteristics.

Naturally developing disturbances in the very unstable wake exhibit a certain natural drift or intermittency. To eliminate this natural intermittency, the previous experimental investigations of disturbance characteristics in free boundary-layer flow employed artificial excitations. As these investigations (Sato 1960; Sato & Kuriki 1961; Freymuth 1966) were conducted in air, the excitation was achieved by means of a loudspeaker that is tuned to the natural disturbance frequency. The loudspeakers have been positioned upstream of, downstream of, and transverse to the various test sections for the purpose of locking the disturbance into its natural frequency. The locking-in phenomena eliminated the undesirable 10 % drift observed in the natural disturbance frequencies. Although the levels of this artificial excitation are reportedly 'small', it is felt that such excitation should be carefully examined with regard to its probable unnatural effects. For instance, with the entire flow field oscillating with the loudspeaker frequency, it is plausible that the development of the disturbance and its inherent interaction with the mean flow could be radically

different from that observed in the natural flow. Consequently, the present experiment was conducted in water where, with the markedly reduced levels of natural drift and with considerable patience, naturally developing disturbance characteristics were measured.

From the dominant disturbance characteristics obtained from the theory, the distributions of the perturbation velocity, vorticity and Reynolds stress were examined. For the mode I disturbances, which were found to be predominant in the real wake, there exists an oscillating component of perturbation vorticity near the wake centre-plane throughout the wake region examined. Moreover, two secondary peaks in the perturbation-vorticity distribution were noted. These secondary peaks were located symmetrically with respect to the wake centre-plane, just outside the two critical layers, and were in phase with each other but of opposite phase with the component lying on the wake centre-plane. In light of the theoretical prediction that these two secondary components of vorticity experience a spatial amplification twice that of the component on the wake centre-plane, a mechanism is suggested to describe the eventual development of the vortex street. This mechanism indicates that the superposition of the disturbance vorticity upon that of the mean flow gives rise to vorticity concentrations located off the wake centre-plane. As these concentrations have the proper relative rotational characteristics and the appropriate alternate spacing, the conclusion is drawn that the classic von Kármán vortex street formed behind streamlined bodies has its origins in the near wake region. Furthermore, the initial stages of development are predicted by the linear spatial stability theory.

This mechanism is suggested in contrast to that of Sato & Kuriki (1961). According to their interpretation, the vortex street is developed through the transverse displacements of a single row of vortices that originally lie along the wake centre-plane. As these vortices become strengthened in their downstream development, they are displaced alternately in transverse directions. According to their induced velocity fields, they finally stabilize in the configuration known as the classic vortex street. It appears that they mistook the appearance of the second harmonics as a manifestation of the vorticity concentration of the centre-plane. Nevertheless, further experimental investigations of the non-linear development are highly desirable.

The Reynolds stress distributions for the most highly amplified spatial waves indicate that at the most upstream wake stations there is a transfer of energy from the disturbance motion to the mean motion. This transfer takes place only near the wake centre-plane and persists through wake station $x/L = 0{\cdot}05$, thereby tending to stabilize the disturbance motion in this region. Beyond wake station $x/L = 0{\cdot}05$, the Reynolds stress distributions indicate that throughout the cross-stream direction, energy is transferred to the disturbance motion from the mean flow.

Qualitative differences occur between the Reynolds stress distributions of the spatial and the temporal eigenmodes. Consequently, these two viewpoints are not equally capable of describing the wake instability, as postulated by Gaster (1965). Gaster's conclusion was based only upon spatial and temporal analyses of the single Gaussian wake profile used by Sato & Kuriki (1961), for which it just

happens that the two viewpoints predict almost identical characteristics for the dominant disturbance.

Therefore, it is concluded that stability analyses in highly unstable free boundary-layer flows should be done spatially. In addition, the longitudinal variation of these continuously developing mean-velocity profiles has to be taken into account in light of the significant effects attributed to the saddle-point behaviour in the eigenvalue planes.

The authors would like to acknowledge with sincere appreciation the helpful discussions during the course of this work with Dr F. R. Hama and the support of the Mechanics Division of the Air Force Office of Scientific Research. This work was supported by the United States Air Force of Scientific Research under contract AF 49(638)-1656.

REFERENCES

BETCHOV, R. & CRIMINALE, W. O. 1966 Spatial instability of the inviscid jet and wake. *Phys. Fluids*, **9**, 359.

BETCHOV, R. & CRIMINALE, W. O. 1967 *Stability of Parallel Flows*. Academic.

BETCHOV, R. & SZEWCZYK, A. A. 1963 Stability of a shear layer between parallel streams. *Phys. Fluids*, **6**, 1391.

CURLE, N. 1957 On hydrodynamic stability in unlimited fields of viscous flow. *Proc. Roy. Soc.* A **238**, 489.

FREYMUTH, P. 1966 On transition in a separated laminar boundary layer. *J. Fluid Mech.* **25**, 683.

GASTER, M. 1963 A note on a relation between temporally increasing and spatially increasing disturbances in hydrodynamic stability. *J. Fluid Mech.* **14**, 222.

GASTER, M. 1965 The role of spatially growing waves in the theory of hydrodynamic stability. *Prog. Aeron. Sci.* **6**, 251.

GASTER, M. 1968 Growth of disturbances in both space and time. *Phys. Fluids*, **11**, 723.

GASTER, M. & DAVEY, A. 1968 The development of three-dimensional wave-packets in unbounded parallel flows. *J. Fluid Mech.* **32**, 801.

GOLDSTEIN, S. 1929 Concerning some solutions of the boundary layer equations in hydrodynamics. *Proc. Camb. Phil. Soc.* **26**, 1.

MATTINGLY, G. E. 1962 An experimental study of the three-dimensionality of the flow around a circular cylinder. *Inst. Fluid Dyn. Appl. Math., University of Maryland. Tech. Note*, BN-295.

MATTINGLY, G. E. 1966 The hydrogen-bubble visualization technique. *David Taylor Model Basin Rep.* no. 2146.

MATTINGLY, G. E. 1968 The stability of a two-dimensional incompressible wake. *Dept. Aerospace Mech. Sci., Princeton University*, Rep. no. 858.

SATO, H. 1960 The stability and transition of a two-dimensional jet. *J. Fluid Mech.* **7**, 53.

SATO, H. & KURIKI, K. 1961 Mechanism of transition in the wake of a thin flat plate placed parallel to a uniform flow. *J. Fluid Mech.* **11**, 321.

TANEDA, S. 1963 The stability of two-dimensional laminar wakes at low Reynolds numbers. *J. Phys. Soc. Japan*, **18**, 288.

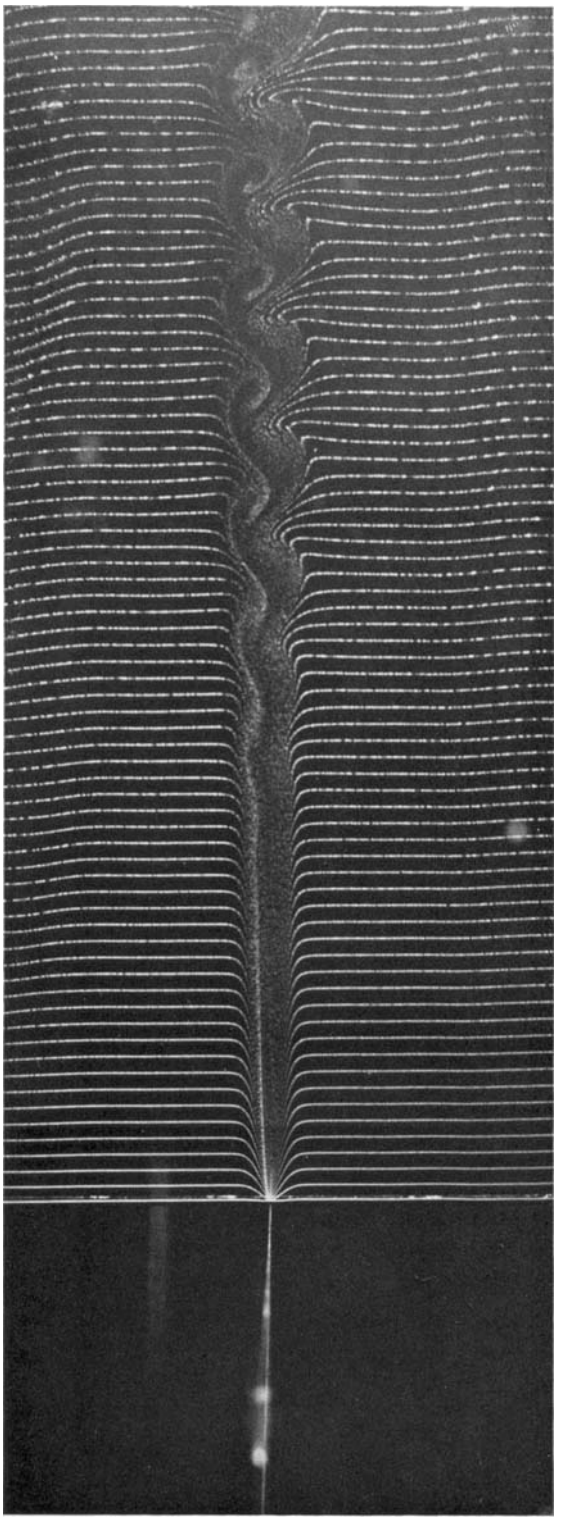

FIGURE 1. Wake flow patterns visualized with hydrogen-bubble technique. Flow is left to right with bubble generating wire supported vertically through the wake 0·0167 in. downstream of trailing edge.

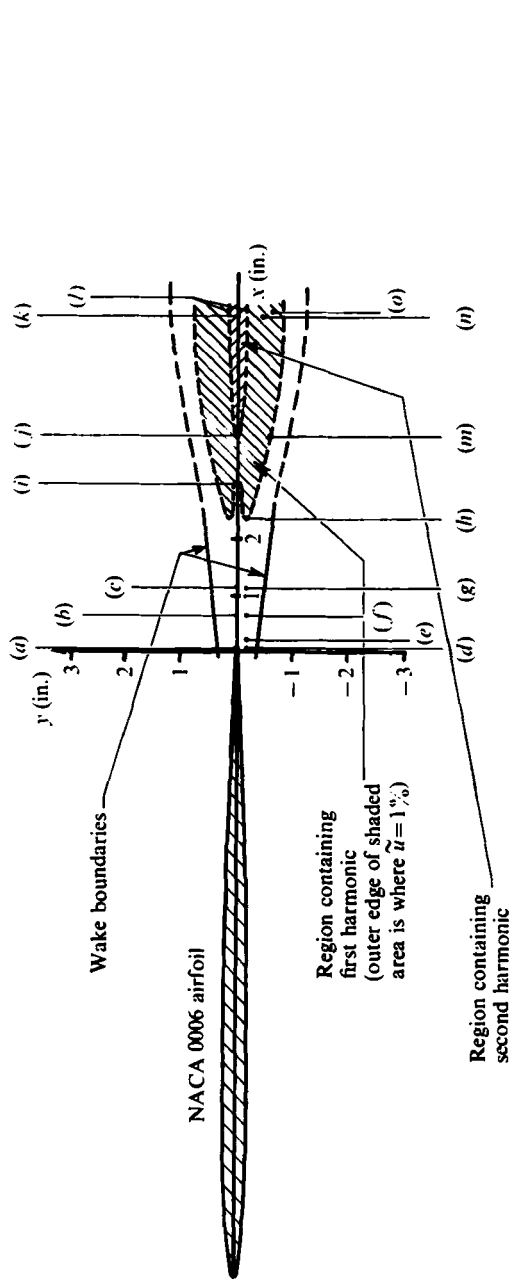

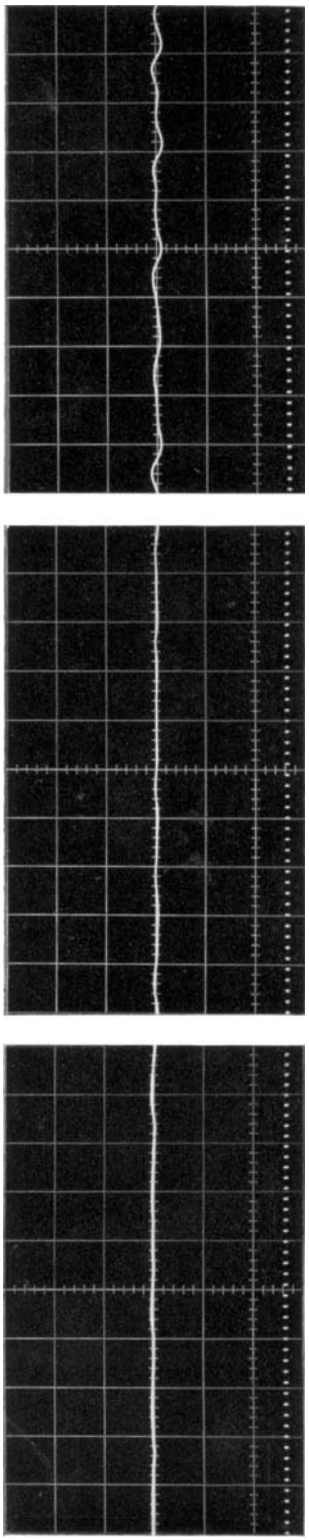

(*a*) 0·0125 (*b*) 0·0125 (*c*) 0·0125

FIGURE 2. Fluctuation map. The decimal under each oscillograph is the amplitude of $\tilde{u}$ per grid size; the dots at the bottom of each oscillograph are 0·1 sec apart.

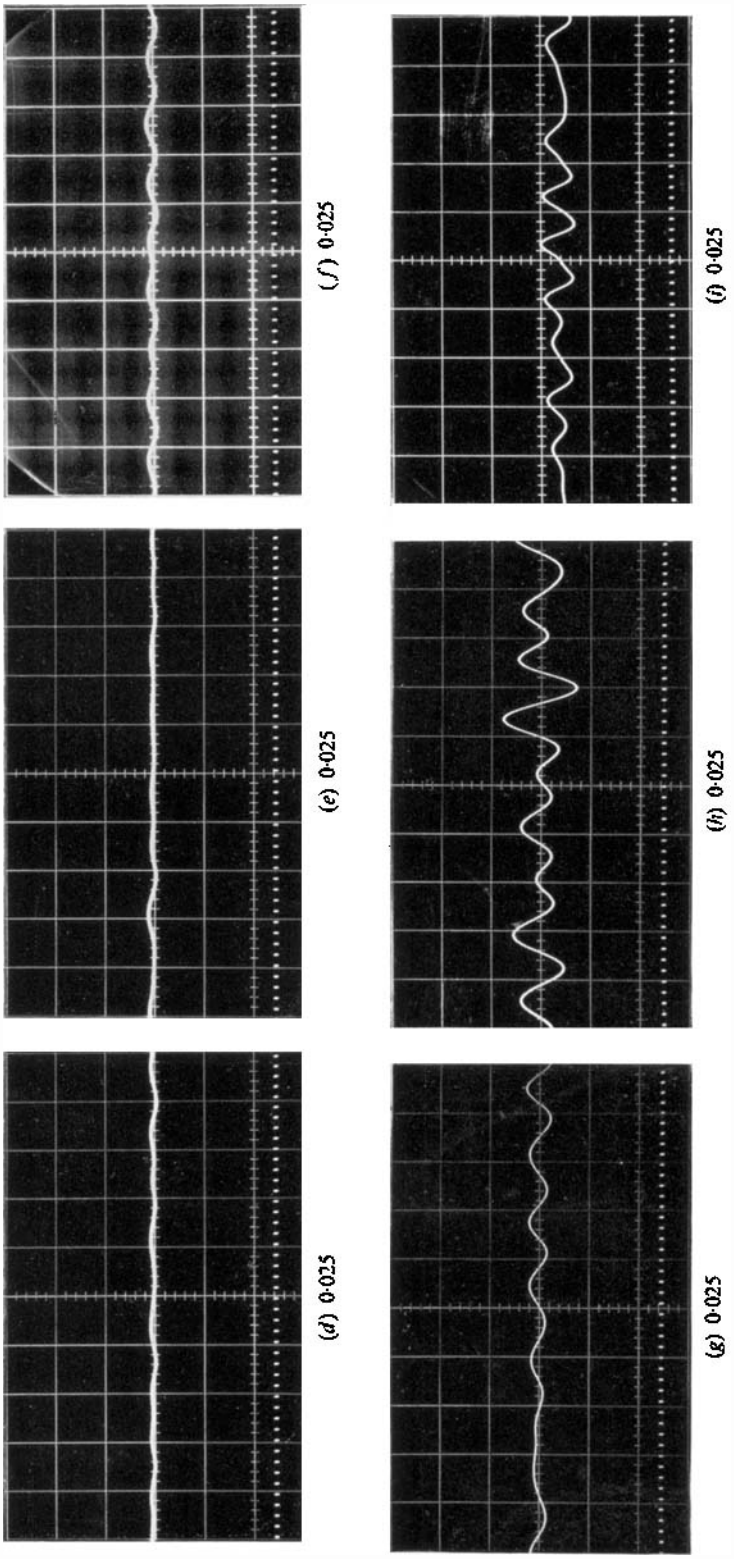
(f) 0·025
(i) 0·025
(e) 0·025
(h) 0·025
(d) 0·025
(g) 0·025

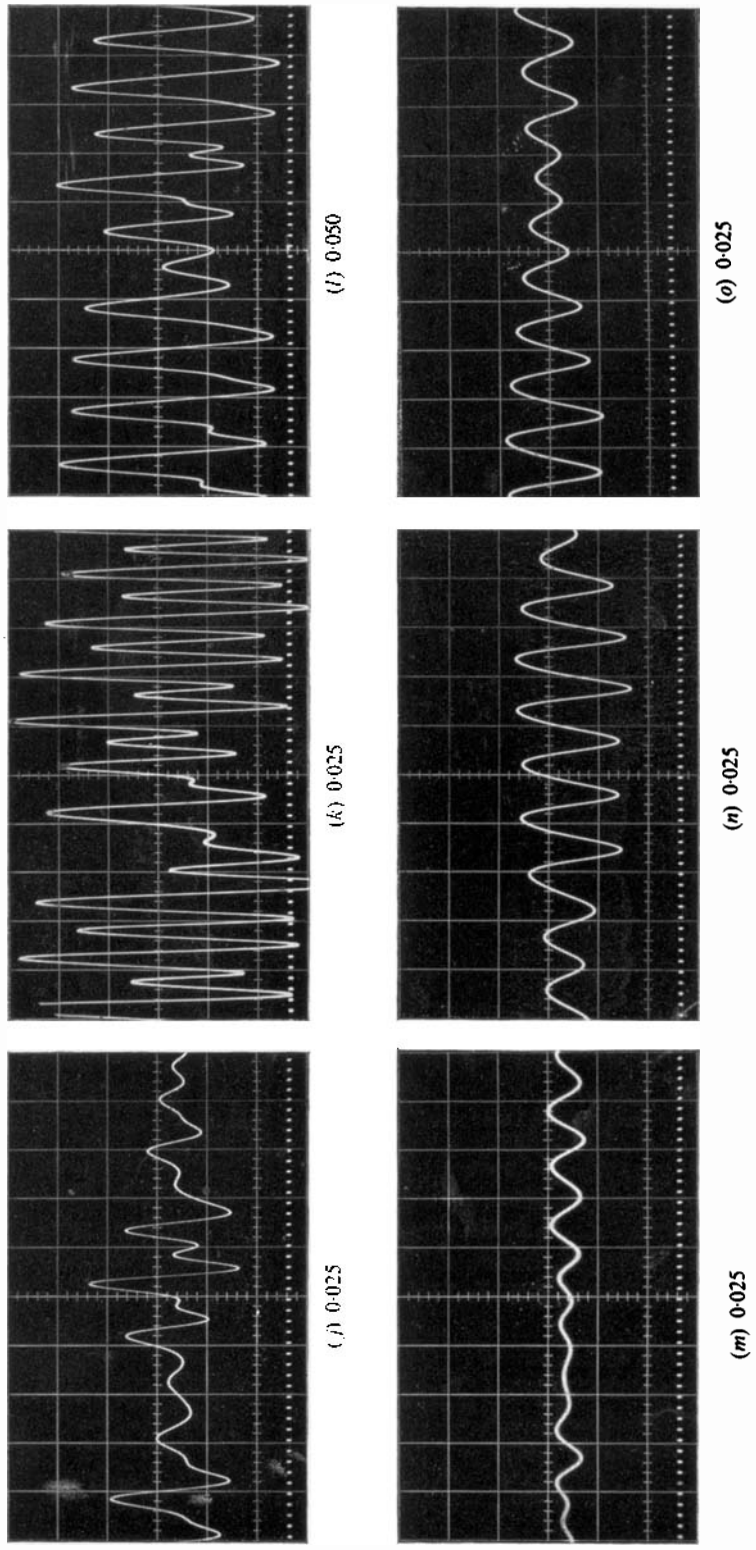
(l) 0·050
(o) 0·025
(k) 0·025
(n) 0·025
(j) 0·025
(m) 0·025